Flow-assembled Chitosan Membranes in Microfluidics: Recent Advances and Applications

Journal:	*Journal of Materials Chemistry B*
Manuscript ID	TB-REV-01-2021-000045.R1
Article Type:	Review Article
Date Submitted by the Author:	16-Feb-2021
Complete List of Authors:	Ly, Khanh; Catholic University of America, Biomedical Engineering Hu, Piao; Catholic University of America, Mechanical Engineering Pham, Phu; Catholic University of America, Mechanical Engineering Luo, Xiaolong; Catholic University of America, Mechanical Engineering

ARTICLE

Flow-assembled Chitosan Membranes in Microfluidics: Recent Advances and Applications

Khanh L. Ly[a], Piao Hu[b], Le Hoang Phu Pham[b], and Xiaolong Luo[b*]

Received 00th January 20xx,
Accepted 00th January 20xx

DOI: 10.1039/x0xx00000x

The integration of membranes in microfluidic devices has been extensively exploited for various chemical engineering and bioengineering applications over the past few decades. To augment the applicability of membrane-integrated microfluidic platforms for biomedical and tissue engineering studies, a biologically friendly fabrication process with naturally occurring materials is highly desired. The in-situ preparation of membranes involving the interfacial reactions between parallel laminar flows in microfluidic networks, known as the flow-assembly technique, is one of the most biocompatible approaches. Membranes of many types with flexible geometries have been successfully assembled inside complex microchannels using this facile and versatile flow-assembly approach. Chitosan is a naturally abundant polysaccharide known for its pronounced biocompatibility, biodegradability, good mechanical stability, ease of modification and processing, and film-forming ability near-physiological conditions. Chitosan membranes assembled by flows in microfluidics are freestanding, robust, semipermeable, well-aligned in microstructure, and highly affinitive to bioactive reagents and biological components (e.g. biomolecules, nanoparticles, or cells) that provide facile biological functionalization of microdevices. Here, we discuss recent developments and optimizations in the flow-assembly of chitosan membranes and chitosan-based membranes in microfluidics. Furthermore, we recapitulate the applications of the chitosan membrane-integrated microfluidic platforms dedicated to biology, biochemistry, and drug release fields, and envision the future developments of this important platform with versatile functions.

Keywords: Chitosan membrane (CM); chitosan-based membrane (CBM); microfluidics; flow-assembly; developments; applications.

1 Introduction

Microfluidics has been intensively applied in a variety of analytical, bioengineering, and chemical engineering studies thanks to its low reagent consumption and fabrication cost, quick reaction time, and high sensitivity and controllability [1, 2]. Integrated microfluidic platforms for life science applications demand enhanced biocompatibility and biological functionality. Towards biofunctionalization of microdevices to minimize their intrinsic difference from biological components, the utility of an environmentally friendly synthesising process with biocompatible materials is highly desired [3, 4]. Membrane technology offers a precise separation process with various driving forces (e.g., concentration gradient, electrical force, pressure difference, and thermal variation) in a cost-saving, operation-efficient, and function-versatile manner as compared to traditional separation techniques [2, 5]. The integration of membrane functionality into microfluidics has converged their inherent advantages for broader applications [6].

There are several options to integrate membranes into microfluidic networks with respective pros and cons for each. Direct incorporation of the commercial membrane to microdevices is problematic due to insufficient sealing and unwanted leakage that can lead to chemical compatibility issues. The preparation of the membrane as a part of the microdevices fabrication process is complicated and exorbitant [7, 8]. *In-situ* preparation of membrane in microfluidic networks, stemmed from interfacial reactions between converging laminar flows and referred to as the flow-assembly technique, has emerged as a promising alternative [9-11]. The accurate manipulation of multiphase flows in microfluidic networks enables a highly programmable formation of a wide range of polymeric membranes such as alginate [12], chitosan [3, 13], nylon [14, 15], palladium-complex [16], and polyacrylamide [17] membranes. Among them, freestanding chitosan membrane (CM) or chitosan-based membrane (CBM) assembled by flows inside microfluidic devices are the prominent candidates to integrate biology to inorganic devices thanks to its favorable offerings, which is the subject of the present review.

Chitosan is a derivative of the secondly abundant biopolymer chitin that comprises of linear N-acetyl glucosamine and β-1,4-linked D-glucosamine units. Owing to its pronounced biocompatibility, biodegradability, low cost, ease of modification and processing, non-toxicity, and good absorption properties, chitosan has been broadly applied for a diverse range of biomedical, bio-microelectromechanical systems (bioMEMS), tissue engineering, and drug delivery applications [18-21]. Besides the mentioned biological and physiochemical significance, chitosan has been eminent for its pH-dependent solubility. Chitosan is water-soluble in acidic conditions and becomes insoluble with gel-forming properties when pH of the surrounding environment is higher than its pKa (~6.3), making its gelation closed to physiological conditions. Therefore, chitosan is an

---

[a] *Department of Biomedical Engineering, The Catholic University of America, Washington, D.C. 20064, USA.*
[b] *Department of Mechanical Engineering, The Catholic University of America, Washington, D.C. 20064, USA. E-mail: luox@cua.edu; Tel: +1 202 319 6952*

ideal candidate for biological and biomedical applications [22, 23]. Most importantly, its abundant amine groups enable the undemanding immobilization of bioactive reagents (e.g. biomolecules, other polymers, or nanoparticles) and biological components (e.g. cells or tissues) to the chitosan backbone [24], thus augmenting the biocompatibility and bioactivity of the chitosan-integrated microchips.

Previous review articles have explored the uses of chitosan in bioMEMS applications [24] and membrane technology [5], CMs in separation applications [25], and CMs as absorptive membranes [26]. Common strategies to integrate CM to microdevices including solution casting, spin casting, electrodeposition, and nanoimprinting have also been recapitulated [24, 27]. To the best of our knowledge, no review paper has yet been dedicated to reporting the flow-assembly of CMs and CBMs and their integrated microfluidic platforms for practical applications. As depicted in scheme 1, the precise control of two fluidic flows, specifically an acidic chitosan solution and a basic buffer solution, inside microchannels enables the versatile, rapid, and reliable formation of CM as desired in microchips. The flow-assembled CM is freestanding, semi-permeable, robust, well-aligned in microstructure [3, 13, 28], and easy to decorate with bioactive reagents [7, 29-34]. In this review, we commence with a general explanation of the formation mechanism of flow-assembled CM in Section 2. Next, Section 3 reports the characteristics of flow-assembled CM, followed by a summary of recent advances and modifications in the flow-assembly of CM and CBM in microfluidics in Section 4. Lastly, Section 5 discusses the implementations of the CM-integrated microfluidic platforms in diverse applications ranging from biochemistry to biology to drug release screening. We envision that flow-assembly of CM will emerge as an important platform and have tremendous benefits for multidisciplinary applications, and this timely review article can aid in directing the future developments of this platform.

2 Flow-assembly of chitosan membranes in microfluidics

Chitosan is a polysaccharide containing many amine groups that are protonated in low pH environment, making chitosan water-soluble. As the surrounding pH value rises higher than chitosan's pK_a around 6.3, the amine groups on chitosan are deprotonated, inducing a sol-gel transition to form hydrogel or membrane-like structure as depicted in Figure 1A(a) [38]. Based on this unique pH-responsive property of chitosan, it is possible to assemble CM in microdevices by a localized pH gradient at the flow interface with the flow-assembly technique [23]. In general, there are two tactics with variations and further optimizations to flow-assemble CM in microfluidic channels, as discussed below.

The first *in-situ* fabrication of CM in microfluidics was demonstrated at the converging flow interface between an acidic chitosan solution and a basic buffer solution, where a stable pH gradient was established at the flow interface to directly assemble a CM as illustrated in Figure 1A. The established pH gradient was visualized by adding pH indicator in the middle microchannel as demonstrated in Figure 1A(b). A well-distinguished pH gradient transitioning from pH of 4 (pink) to pH of 10 (blue) was established where the two fluidic streams converged, triggering the sol-gel transition of chitosan, and ultimately forming a CM at the interface. The formation of freestanding CM commenced from the upstream nucleation point and propagated to the downstream anchoring point situated [3, 23]. Figure 1A(c) shows a 60-µm-thick CM formed along the interface of the two converging flows of acidic chitosan and basic buffer solutions. The fabricated CM was usually long (up to 4 mm) and thick in this scenario. The key to the successful CM formation was to establish stable pH gradients at the flow interface with an appropriate device design and pumping strategy. One challenge of this direct assembly approach was the deposition of chitosan residues in the downstream channels, which could disrupt the

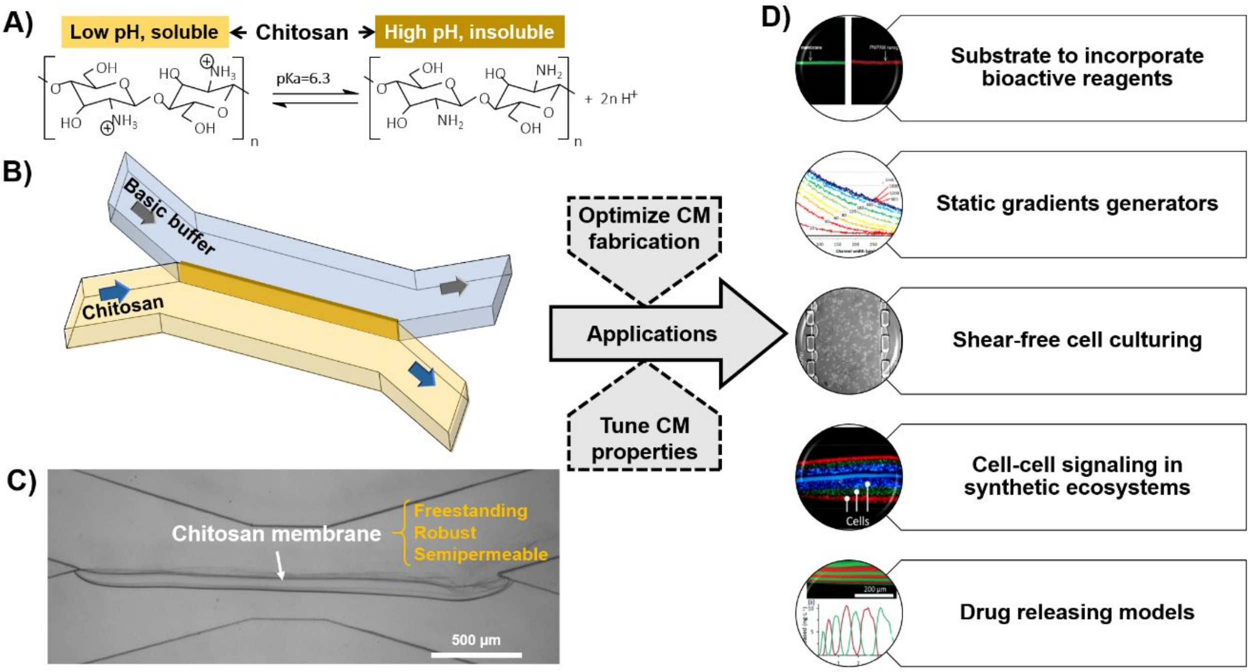

Scheme 1: Flow-assembled chitosan membrane (CM) in microfluidics. **(A)** Molecular transition of chitosan around its pKa at 6.3. **(B)** Flow-assembly of CM between parallel flows. **(C)** Key features of the assembled CM. **(D)** CM in microfluidics for versatile applications. Adapted with permission from references [3, 30, 35-37].

pressure balance between the flow streams and dislocate the membrane anchoring on device. One solution to this challenge will be further discussed in Section 4.

Figure 1B shows the second approach to flow-assemble CM involving the use of alginate in the basic solution. This approach utilized an air bubble to initiate the biofabrication of a CM on a thin polyelectrolyte complex membrane (PECM), which was generated as the alginate and the chitosan solutions came into contact [13]. The PECM was spontaneously formed upon electrostatic interactions between the negatively charged carboxyl groups of alginate chains and the positively charged amino groups of chitosan chains as depicted in Figure 1B(a). The PECM acted as a barrier to prevent the diffusion of either alginate or chitosan chains, evidenced by a clear interface established between a drop of chitosan solution and a drop of alginate solution (Figure 1B(b)). The ionic reaction between the alginate and chitosan solutions to form a PECM in a microfluidic device as depicted in Figure 1B(c-e). Chitosan and alginate solutions were slowly introduced into two separate microchannels, whilst one set of outputs was blocked, and the other set of outputs were connected by an air-filled tubing (Figure 1B(c-d)). Initially, as chitosan and alginate solutions came near the aperture, an air bubble was trapped within the aperture due to the hydrophobicity of the polydimethylsiloxane (PDMS) device (Figure 1B(e)-(i)). Then, the pressure between the flow fronts of the alginate and chitosan solutions was balanced through the air-filled tubing. Continuous pumping of the solutions increased the pressure inside the microchannels, which dissipated the trapped air bubble through the gas-permeable PDMS layer, and the alginate and chitosan solutions finally came into contact and spontaneously formed a PECM at the solution interface (Figure 1B(e)-(ii)). Once the PECM was formed, the CM was built upon the PECM with the localized pH gradient generated by the continuous diffusion of hydroxyl ions from the alginate side via the PECM (Figure 1B(e)-(iii)) [13]. This approach enables the formation of a relatively shorter and thinner CM than the one assembled directly at the flow interface. The microchip pattern with the long flow interface is no longer required to maintain the stable localized pH gradient, which allows more room for customization and optimization of microchip design for broader applications [13, 29, 35, 39-42]. It is important to note that the addition of PECM introduces

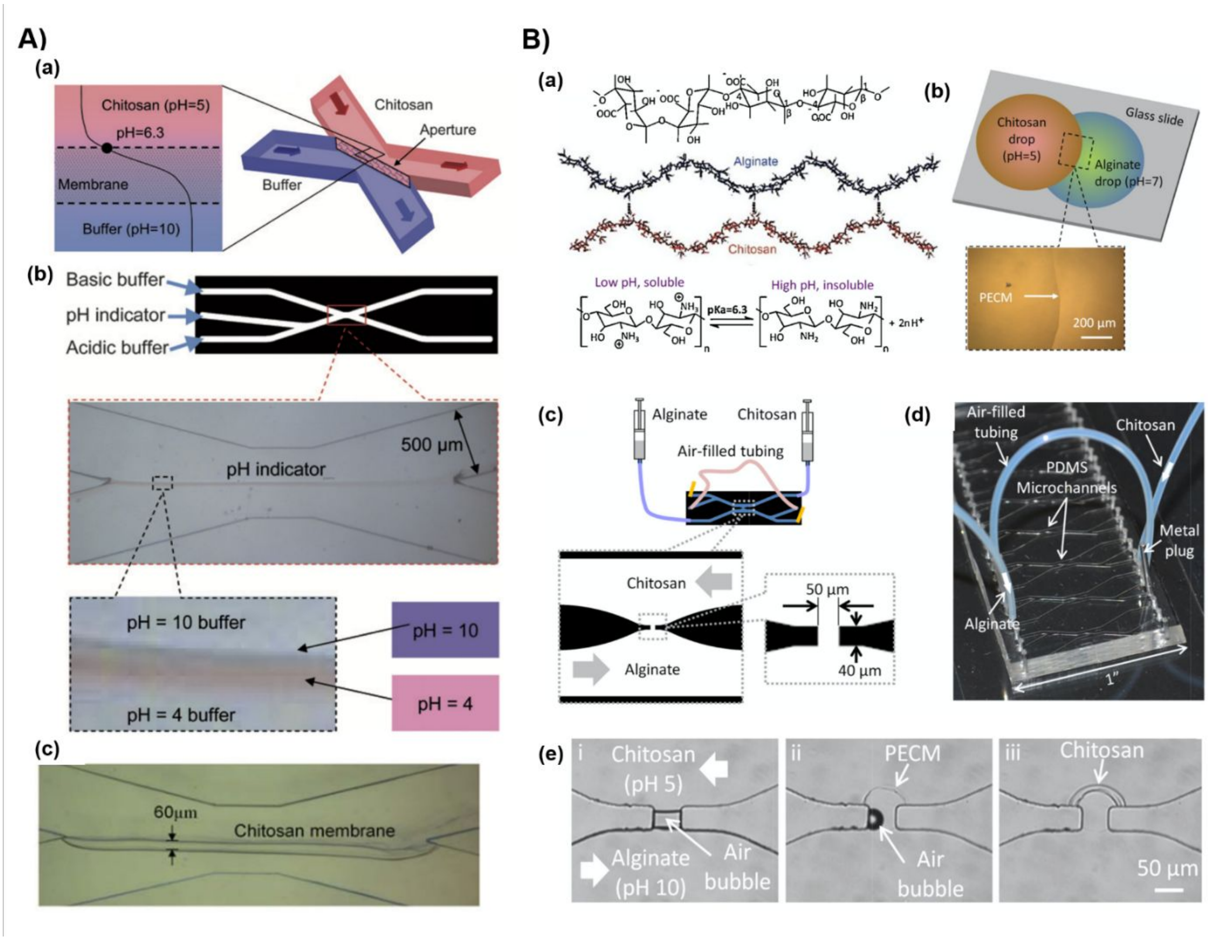

Figure 1: Mechanisms for the flow assembly of CM in microfluidics. **(A)** Direct gelation with basic buffer: (a) Schematic of CM formation with a localized pH gradient established at the flows interface of a basic buffer and acidic chitosan solutions; (b) Microfluidic device design and the pH gradient generated at the flows interface in microchannels, visualized with a pH indicator solution; and (c) The microscopic image of a fabricated CM. **(B)** Gelation across a polyelectrolyte complex membrane (PECM) layer: (a) Chemical structures and electrostatic interactions between alginate and chitosan chains; (b) the formation of PECM at the interface of an alginate solution drop and a chitosan solution drop; (c) Experimental setup to balance pressure and expel a naturally trapped air bubble in a hydrophobic PDMS aperture between two microchannels; (d) A PDMS device containing several microchannels bonded to a glass slide; and (e) Dissipation of air bubble and formation of the permeable PECM allowing for hydroxyl ions to diffuse through PECM, and ultimately, form CM. 1A is adapted with permission from The Royal Society of Chemistry [3]; 1B is adapted with permission from Elsevier [13].

carboxyl groups in alginate chains to one side of CM besides the already existing amine groups inside and on the surface of CM, thus expanding the capability to immobilize versatile biomolecules onto CM using either amine or carboxyl chemistry. The contribution of PECM in protecting the alginate hydrogel with embedded cells will also be discussed in section 5.

3 Characterizations of flow-assembled chitosan membranes

3.1 Physicochemical properties of flow-assembled chitosan membranes

To better utilize the flow-assembled CM-integrated microfluidic platforms, it is critical to understand the characteristics of the fabricated CM. This section reviews the key physicochemical properties of the flow-assembled CM and how some of these properties might change in relation to the fabrication conditions.

First and foremost, the impact of the flow rates on the growth of the fabricated membranes was studied. Figure 2A(a-b) shows that as the flow rate of buffer solution was fixed while varying the flow rate of the chitosan solution and vice versa, respectively, no significant effect on membrane thickness was observed. Meanwhile, Figure 2A(c) reveals that if there was a significant difference in flow rates of basic and chitosan solution, an increase in the total flow rate during fabrication resulted in a significant drop in membrane thickness [31]. The increase in flow rates likely narrows the pH gradient and the time it appears at the interface. Further, the faster the flow rates, the higher the shear stresses emerge at the membrane surface, the shorter time for the chitosan chains to anchor, ultimately leading to thinner and denser membranes [43, 9]. Therefore, it is possible to control the thickness of the flow-assembled CM by varying the total flow rates while maintaining the flow rate ratio between basic and chitosan solutions.

Second, Luo et al. investigated the average pore size of the fabricated CM through permeability tests with fluorescein isothiocyanate (FITC), tetramethylrhodamine (TRITC)-labelled antibodies, and FITC-labelled polystyrene nanospheres, among which the particle size ranged from less than 1 nm to 20 nm in diameter. Figure 2B(b, c, e) shows that the fluorescein (less than 1 nm in size) freely passed through, TRITC-labelled antibodies (size of 7–10 nm) partially diffused through, while FITC-labelled polystyrene nanospheres (20 nm in diameter) were completely stopped by the membrane. The results suggest that the pore size of flow-assembled CM is within the nanometer range around the size of proteins or antibodies [3]. In a later study, Luo and colleagues yielded similar results in the permeability of the flow-assembled CM fabricated using their newly developed air-initiated biofabrication process [13]. In summary, the flow-assembled CM is permeable to small molecules with the molecular weight cut-off of a few nanometers while physically separates flow streams, which can be used as a reaction site for biomolecular immobilization and enzyme catalysis [3, 13, 23].

Third, the microstructure and polymer chain alignment of the fabricated membranes and the contributing fabrication parameters were investigated. Li et al. utilized quantitative polarized light microscopy (qPLM) to examine the birefringence signals and determine the effects of pH and the flow rate on the flow-assembled CM's microstructural organization and polymer chain alignment[28]. Birefringence is an inherent optical property of anisotropic materials that can reveal their crystal microstructures and polymer chain alignment [45]. The qPLM offers a powerful means to study the birefringence of many anisotropic materials by generating optical retardance location maps in relation to the microscale-level organization and alignment of birefringent macromolecules [46]. Optical retardance generated by qPLM digital image processing is a parameter proportionally correlated to birefringence signals of materials where the higher optical retardance represents the higher crystalline and alignment order of materials [47]. Details on how to obtain the optical retardance map of CM can be found in subsection 4.3 and previous reports [28, 29, 39]. Herein, the authors figured out that the flow-assembled CM was highly aligned along the flow direction of the chitosan solution inside the PDMS microfluidic network. Furthermore, the optical retardance signals of the flow-assembled CM increased significantly in relation to the alginate solution's pH, but was less dependent on the flow rates [28]. Notably, the optical retardance signal reduced dramatically from the PECM side to the alginate side of the membrane despite the increased molecular density in the membrane [28]. Shown in Figure 2C(a) is a set of typical CMs after 10 minutes assembled by flows with varied pH values of the alginate solution while the pH of the chitosan solution was fixed. Noticeably, the CM's thickness rose significantly with the increased pH of the alginate solution. Figure 2C(b) displays the corresponding birefringence signals of CMs in (a), which were apparently observed for all CMs assembled in different conditions with a steady decrease in optical retardance across the membrane growth direction. Furthermore, Figure 2C(d) shows that as the alginate solution's pH increased, the higher flux of hydroxyl ions and sharper pH gradient ultimately leaded to higher optical retardance in the CM. On the other hand, the birefringence signal was less sensitive to the variation of the flow rates of the polymer solutions [28].

Fourth, the adhesion strength of the freestanding CM to PDMS device was determined by employing the simple ideal gas law as previously reported. The general principle of the characterization method is shown in Figure 2D(a). By connecting compressible air in a leak-tight syringe with incompressible liquid in the tubing to the microchannel, the hydrostatic pressure acting on the membrane was reflected by the decreased air volume [13, 39, 48]. The relationship between the critical pressure to detach CM from PDMS with the CM thickness is shown in Figure 2D(b-c). The authors reported that a linear correspondence was observed between the critical pressure and the membrane's thickness: the thicker the membrane, the higher the critical pressure. Notably, the typical 54 µm thick freestanding CM could withstand hydrostatic pressure of up to 1.1 atmosphere pressure, suggesting that the anchoring of flow-assembled CM on PDMS are robust [13]. It is worth pointing out that so far only the adhesion strength of CM onto PDMS was characterized, while the intrinsic mechanical properties of flow-assembled CM are yet to be further investigated. Presumably, CM can be fabricated in pure PDMS microchannel by replacing the bottom glass slide with a planar PDMS, so that the fabricated CM can be harvested for further characterization.

Lastly, since chitosan is a well-known pH-responsive biopolymer, the flow-assembled CM also possesses this respective property. The deprotonation of chitosan amine groups to transit soluble chitosan chains into insoluble CM at pH higher than 6.3 is reversible. This means the insoluble CM can be readily dissolved if the pH of surrounding environment falls below 6.3. Therefore, once the fabrication is completed, the CM must be maintained in aqueous environment with pH higher than its pK_a. It is reported in previous studies that CM was quickly dissolved by half within 20 seconds when an acidic solution with pH of 2 was introduced into the microchannels [39]. It should be noted that in the presence of PECM, formed through the electrostatic interactions between the positively charged amine groups on chitosan chains and the negatively charged carboxyl groups on alginate chains, the CM exhibits complex degradation behavior. The bonds presented in PECM are highly stable at physiological pH yet become labile at mild acidic conditions. Specifically, at pH around 5.5, insoluble CM will be protonated and becomes free positively charged amino groups, leading to a swelling,

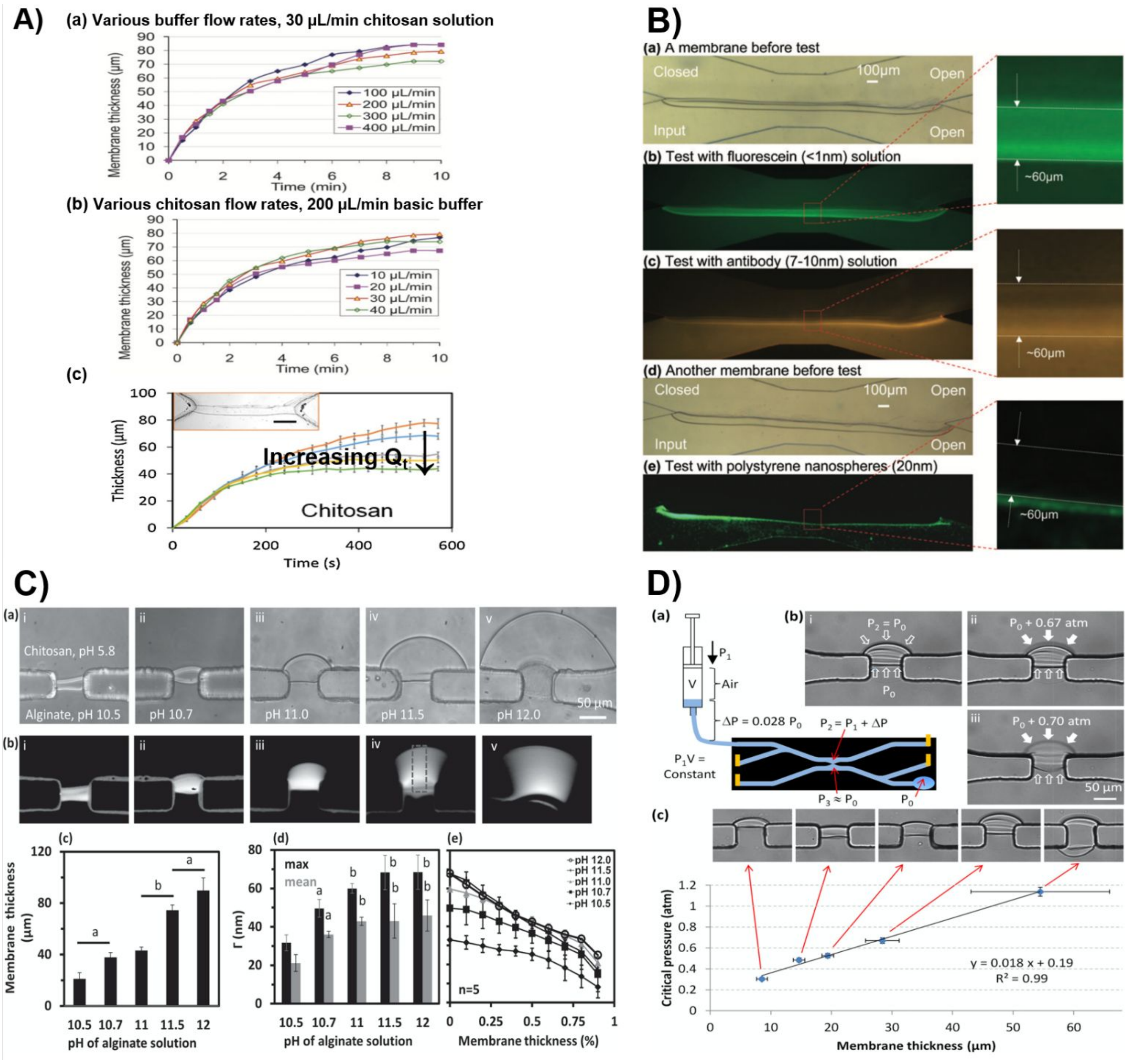

Figure 2: Key physicochemical properties of the flow-assembled CM in microfluidics. (A) Growth curves of CM formed with direct gelation between adjacent flows: Time-dependent growth of membrane thickness at (a) varied chitosan flow rates with a fixed 200 μL/min buffer solution; (b) varied buffer flow rates with a fixed 30 μL/min chitosan solution; and (c) Membrane growth tested under five different total flow rates (Q_t): 2.7 (orange), 5.4 (blue), 8.1 (gray), 10.8 (yellow), and 13.5 mL/h (green). Q_t = the basic solution's flow rate (Q_b) + the chitosan solution's flow rate (Q_p) and the ratio of Q_b/Q_p = 20; (B) Permeability of CM formed with direct gelation: (a, b) free diffusion of FITC (molecular size <1 nm); (c) partial transport of TRITC-labeled antibody (molecular size of 7–10 nm); and (d, e) complete stop of FITC-labeled polystyrene nanospheres (particle size of 20 nm). (C) The birefringence of CM formed across PECM: (a) & (c) the membrane thickness, (b) & (d) the birefringence signals, and (e) the birefringence across the normalized membrane thickness of CM formed with gelation across PECM at various alginate solution pH of 10.5, 10.7, 11.0, 11.5, and 12. (D) Adhesion strength characterization of CM formed with gelation across PECM using the ideal gas law principle: (a) Experimental setup; (b) Pressure measurement of an approximately 30 μm thick CM before it burst at 0.67 atm pressure; and (c) Critical pressure in linear relationship to membrane thickness. 2A(a, b) and 2B are adapted with permission from The Royal Society of Chemistry [3]. 2C is adapted with permission from IOP Publishing [28]. 2A(c) and 2D being adapted with permission from Elsevier [13, 31].

then gradual degradation of the CM [49]. Such responses of CM to pH of surrounding environment can be utilized for controlled drug release and will be described in Section 5.5. In another scenario, if the pH falls below 3.5, the pK_a of alginate, the CM experiences faster degradation while the alginate becomes insoluble, resulting in a remaining PECM structure as previously reported [50, 51]. On the other hand, CM can also be crosslinked with glutaraldehyde or terephthalaldehyde to improve the strength and acidic resistance for more diverse applications [30, 39].

3.2 Characterization approaches for flow-assembled chitosan membranes

Due to their tiny size, it is challenging to determine the characteristics of CM in microfluidic device [55]. In this section, we will list the most used approaches to characterize the physicochemical properties of flow-assembled CM and CBM.

One most convenient spectroscopic approach to visualize CM and CBM in a microfluidic chip is fluorescence microscopy. Flow-assembled CM can be readily recognized under transmitted light microscopy, while chitosan molecules can also be conjugated with fluorescein to distinguish it from other polymers [13]. Further, using fluorescence microscopy, fluorescent dyes can be conjugated to biomolecules to confirm the presence or visualize their distribution within the fabricated membranes [30, 37]. Fluorescence microscopy also aids to characterize the permeability of CM [3, 13], CBM [30], modified CM [7, 29, 39, 55], and the generated chemical gradients [29, 35, 52]. Most importantly, the fluorescence microscopy technique is compatible with most microfluidic devices and can provide real-time observation and assessment of membrane fabrication and functionalities.

Further, it is also challenging to determine the microstructural organization of the fabricated membranes in microchip using conventional characterization methods due to the tiny size of the structure [24, 55]. Therefore, advanced spectroscopic techniques such as qPLM and scanning electronic microscopy (SEM) have also been used for the membrane characterizations. To obtain optical retardance correlated to birefringence of the CM, images of the membrane under sequent analyzer angles are taken with the birefringence signal of interest as CM goes from the brightest to the lowest. The optical retardance map of the membrane is then obtained by fitting the birefringence signal versus analyzer angle to a second-order polynomial [28, 29, 39]. SEM can also be employed to image the subnano- or microscale morphology of the CM and CBM. However, a specialized sample must be prepared for SEM observation since the conventional microfluidic devices are strongly bound and do not allow the electron beam to penetrate through. Furthermore, the specialized sample must possess good electrical conductivity to obtain high-resolution images. To facilitate the extraction of the fabricated CM and CBM for SEM observation, specialized microfluidic devices can be fabricated with PDMS microfluidic channels as the top layer, and tape [7, 56] or PDMS [29] as the bottom layer (PDMS-tape or bilayer PDMS devices, respectively). Additionally, to enhance the conductivity of the sample, the colloidal silver liquid can be added around the sample as a ground connector [29], or a PDMS-silicone glass device can be used [57].

4 Developments and optimization in the flow-assembly of chitosan membranes

With the growing interest in the flow-assembled CM and CBM in microfluidics, more and more developments and optimization have emerged in the literature. Table 1 summarizes the main advances that have been reported in the literature and their main purposes. When the flow-assembly of CM was initially reported in 2010, an expertise pressure balancing technique through a specific syringe pump strategy was required to establish a stable pH gradient for membrane assembly. The original process is not user-friendly and generally yields a success rate of around 60% even for experienced researchers [41], and it is challenging to ensure a proper membrane attachment at the downstream [53]. Several advances have been developed to enhance the reliability of the flow-assembly process, among which are the employment of an add-on vacuum layer [41], the

Table 1: Summary of recent advances in the flow-assembly of CM and CBM in microfluidics.

Advance	Purposes	Reference
Add-on vacuum layer	To dissipate air bubbles at the aperture(s) through the gas-permeable properties of PDMS to initiate the flow-assembly of CM.	41
Microchips with small circular pillars	To position the initial chitosan meniscuses that can be advanced down by with the introduction of alginate solution, therefore, preventing trapping air bubbles at the aperture(s) and directly enabling the flow-assembly of CM.	52
Extra outlet	To serve as an anchoring point to guide CM formation.	53
Crosslinking CM with glutaraldehyde (GA)	To prevent the disruption of CM and PDMS pillars interaction caused by anti-adhesion agents (i.e. Pluronic F-127), resist acidic dissolution, and improve adhesion strength of CM onto PDMS device.	39
Tuning the CM' porosity with co-assembled nanoparticles as a sacrificial template	To actively manipulate the porosity of the flow-assembled CM inside microchannels, contributing to their semi-permeability and selectivity regarding application needs.	29
In-situ fabrication of poly(N-isopropylacrylamide) (PNIPAM) nanogels containing CM	To utilize chitosan as an embedded substrate to construct the PNIPAM nanogels-containing membrane with self-regulated permeability abilities, thanks to the reversible swelling or shrinking volume transitions in relation to change in temperature and ethanol concentration of PNIPAM nanogels.	30, 54
In-situ fabrication of carbon nanoparticles-chitosan (CN-CS) composite membrane	To incorporate the absorption abilities of carbon nanoparticles (CNs) into chitosan (CS), creating an on-chip CN-CS composite membrane, which can perform absorption and dialysis dual functions.	7
Fabrication of hybrid collagen-chitosan membrane	To construct a potential extracellular matrix-like biomembrane, which possesses the good biocompatibility of collagen and great mechanical strength and processability of chitosan for on-chip cell cultures.	31

use of microchips containing circular pillars [52], and the addition of an extra outlet [53].

Although the flow-assembly of CM offers a rapid, facile, and reliable strategy to integrate biopolymer membrane to microfluidics, the solubility in acidic solutions and low-molecular weight cut-off (a few nanometers) of the flow-assembled CM might limit the applications of CM-integrated microfluidic platforms. To overcome those problems, several studies have attempted to tune the properties of the fabricated CM by crosslinking with glutaraldehyde [39] or tuning its pore size with co-assembled nanoparticles as sacrificial materials [29]. Meanwhile, the main inherent advantage of chitosan is its high affinity to bioactive reagents and biological components for the biological functionalization of microdevices. Studies have exploited this ability of chitosan as a substrate to successfully immobilize bioactive materials such as poly(N-isopropylacrylamide) nanogels [30], carbon nanoparticles [7], or collagen [31] into microfluidics. This enhances the functionality of the synthesized CBM and the applicability of CM-integrated microfluidic platforms for many biological and cellular studies. These developments are discussed further in this section.

4.1 Technical advances in the flow-assembly process

As aforementioned, one challenge of the direct assembly of CM at the flow interface in Figure 1(A) was the deposition of chitosan residues in the downstream channels that could disrupt the pressure balance between flow streams and dislocate the membrane anchoring point. One solution to this challenge was to include an extra acidic input at the downstream connecting to the downstream microchannels as featured in Figure 11A(b). The extra acidic flow continuously cleansed out any deposited chitosan residue and automatically balanced the pressure between the flowing streams. The extra acidic input greatly improved the success rate of CM as the acidic flow rate could be much higher than those of the polymer and basic buffer flow streams, and the flow rates could be adjusted as needed to clean any downstream residues. One drawback of the extra input is that the polymer and buffer flow channels compartmented by CM are no longer physically separated at downstream and limit the applications when complete compartmentalization is desired.

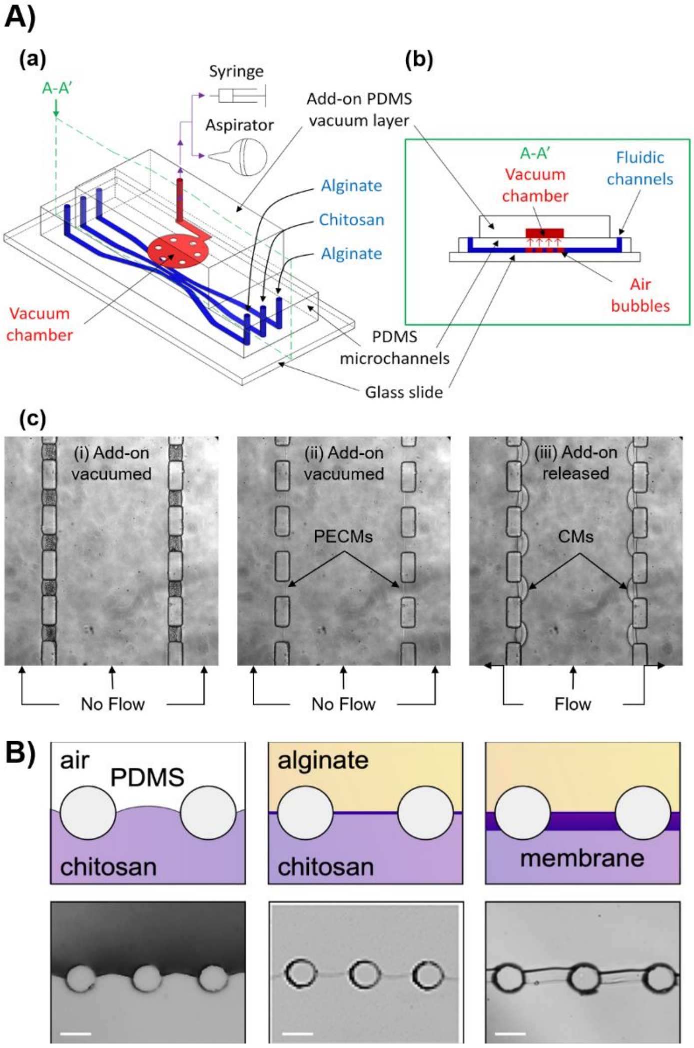

Figure 3: Optimizing the flow assembly of CM technique in microfluidics. **(A)** Gelation across PDMS by dissipating air bubbles trapped at the apertures using an add-on vacuum layer: (a) 3D schematic of a microfluidic chip with an add-on vacuum layer on top; (b) A-A' cross-section showing air bubbles dissipation through PDMS upon vacuuming; and (c) *In situ* biofabrication of arrays of CMs facilitated with the add-on vacuum chamber: (i) air bubbles trapped in the apertures being vacuumed, (ii) air bubbles were dissipated, allowing the interaction between chitosan and alginate macromolecules to form PECMs. **(B)** Direct gelation in PDMS device with small circular pillars: Three stages of the *in-situ* formation of CM without trapping air bubbles. Scale bars: 100 µm. 3(A, B) are adapted with permission from The Royal Society of Chemistry [41, 52].

In addition, it is noticed that the downstream flow in the microchip represented in Figure 1A(c) generally prevents sufficient membrane attachment at the downstream point, therefore, reducing the success rate of CM formation. Thus, to better secure the formation of CM to the downstream point, Tibbe et al. designed a new microchip with an extra outlet, serving as an anchoring point to guide the membrane formation [53]. Furthermore, Jia et al. reported that by using the microchips with low aspect ratio microchannels, the reliability of flow-assembly of CMs can be enhanced. With the use of the low aspect ratio microchannels and by adjusting the flow rate of both flow streams in relation to their viscosity, the pressure at the flow interface can simply be balanced, thus, creating the stable localized pH gradient for the CMs assembly [37].

To improve the reliability of the flow-assembly process in Figure 1(B), a technical innovation using an add-on PDMS vacuum layer as needed was developed to dissipate air bubbles from small apertures. This technical advance utilized the gas-permeable properties of PDMS, the typical material used for microdevices fabrication, to dissipate air trapped in the aperture as schematically depicted in Figure 3A(a-b). Once the air bubble was vacuumed out by withdrawing a connected syringe or a squeezed nasal aspirator (Figure 3A(a)), the chitosan and the alginate solutions came into contact to spontaneously form a PECM, followed by the formation of CM by restarting the flows [13, 41]. The idea to vacuum air trapped inside a small aperture through the PDMS layer was adapted from the de-bubble process reported previously [58], except that the add-on vacuum layer was not plasma bonded to the bottom PDMS microchips. This not only provides a rapid (usually from 9 to 20 minutes) and versatile strategy (applicable to different PDMS microchips) to actively remove air bubble inside microchannels, but also allows the add-on vacuum layer to be reused as many times as possible. Using this technical advance, the success rate of the flow-assembly of CM has been significantly increased to almost 100% for not only experienced users but also recruits. With the easy add-on vacuuming process, arrays of CMs in a three-channel network as in Figure 3A(c) were reliably fabricated with one introduction of solutions [41], which were used for the generation of static gradients and further discussed in Section 5. The CM assembled by this steering air bubble method was well-controlled with flows and pH of the polymer solutions, and the membrane growth curve was similar to that with the pressure-balancing approach [35, 41]. Most importantly, the properties and functionality of the fabricated CM using this newly developed approach remain unchanged: the CM is freestanding and strongly adhered to PDMS device, selectively permeable to small molecules and ions, and chemically communicating between the CM-separating compartments [13, 35].

Meanwhile, Gu et al. reported a modification in microchannel design, through which it was possible to prevent the trapping air bubbles at the apertures, thus, directly enabling the formation of CM. In particular, the authors adapted the previously developed gradient generator design with small circular pillars as schematically illustrated in Figure 3B. By carefully positioning the convex meniscuses that emerged at the apertures when introducing the chitosan solution followed by the introduction of the alginate solution, the authors enabled the direct interaction of the two solutions to form the PECMs without air bubbles intervening [52]. Next, hydroxyl ions continuously diffused from the alginate side via the PECMs to the chitosan side, creating the localized pH gradients for the formation of the arrays of CMs on the PECMs as previously described. However, the effects of the reported procedure on the membranes' growth rate and its versatility to other microchip designs remain unclear and could be an interesting topic for future studies.

4.2 Modification of the flow-assembled chitosan membranes' properties

The flow-assembled CM is freestanding, robust, well-aligned, and semipermeable to small molecules and ions. These unique characteristics have presented the flow-assembled CM as a promising platform for a variety of applications which are mentioned in section 5. Nevertheless, several challenges still exist and remain unresolved until recently. Firstly, the fabricated CM can be easily detached when the PDMS microchip's channels are treated with an anti-adhesion agent, such as Pluronic F-127 for prevention of biomolecular and cellular adsorption on PDMS [39]. Secondly, the flow-assembled CM cannot be used in an aqueous environment where the pH is above 6.3, and 1X phosphate-buffered saline (PBS) is usually needed as a maintenance buffer [3, 13]. Last but not least, the low-molecular weight cut-off of a few nanometers, the size of antibodies, of the flow-assembled CM poses a problem if mass transport of macromolecules is needed [29].

To tackle the first two problems, Hu et al. utilized glutaraldehyde (GA) to crosslink the fabricated CM for enhanced resistance to anti-adhesion agents and acidic environment, and the properties of the GA-treated CM (GTCM) were investigated. First, after treating CM with 10% GA to convert CM into GTCM, no obvious morphological change was observed in the PBS solution (Figure 4A(a)). CM was quickly dissolved in an acidic environment within 20 seconds (Figure 4A(b)-(i-ii)), while for GTCM no shrinking or swelling was observed over an hour under the same circumstances (Figure 4A(b)-(iii-iv)). These findings indicate that the GA crosslinking of CM significantly increased the acidic resistance of GTCM, which can expand the applicability of the CM-integrated microfluidic platforms. Second, the effects of GA treatment on the flow-assembled CM's molecular organization were examined through the measurement of optical retardance. Figure 4A(c) shows the net optical retardance of both CM and GTCM, revealing a significant drop of about 40% after the GA crosslinking. The significant decrease in optical retardance confirmed that GA treatment had impacted the microstructural arrangement of the flow-assembled CMs [39]. Third, the adhesion robustness of GTCM, determined using the pressure measurement approach reported in Luo et al. [13], was noticeably strengthened. Figure 4A(d) shows that the average critical pressures of CM and GTCM before and after being treated with Pluronic F-127. The results suggest that GA crosslinking not only enhances the adhesion strength of pure CM but also counteracts the robustness-compromising effects of Pluronic F-127 treatment [39]. Importantly, no significant change in the membranes' permeability before and after GA crosslinking. Despite the mentioned above offerings, it is worth noting that the GA treatment would consume chitosan's amine groups and could limit the ability to modify the CM with biomolecules and other substances [24]. Additionally, the use of GA as a crosslinker could raise an unwanted biocompatibility issue due to residual crosslinker, therefore, it must be considered carefully before usage.

To improve the applicability of the integrated membranes for mass transport of macromolecules, it is highly appealed that the membranes' porosity can be manipulated according to application needs. Co-assembled polystyrene nanoparticles as a sacrificial template were investigated to manipulate the porosity of the flow-assembled CM for broader applications as schematically depicted in Figure 4B(a). Briefly, CM with polystyrene nanoparticles (CM-np) was flow-assembled in microchannels and treated with GA [59]. Then dimethyl sulfoxide (DMSO) was used to remove the incorporated

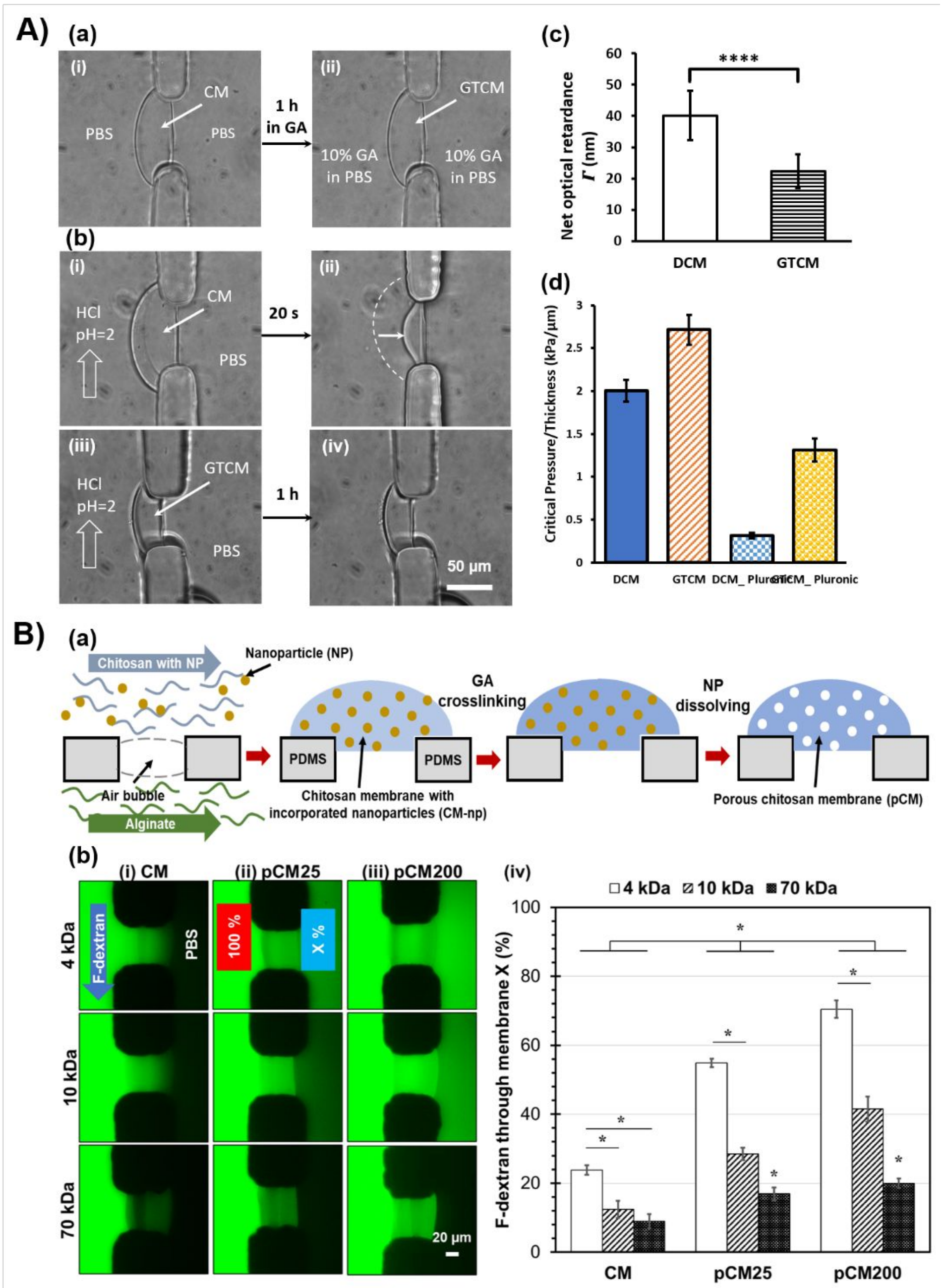

Figure 4: Tuning CM properties. **(A)** Crosslinking CM with glutaraldehyde (GA): (a) No obvious morphological changes between CM and GA-treated CM (GTCM); (b) Acidic resistance of GTCM as compared to CM: (i-ii) CM was dissolved by acidic solution within a few seconds, whilst (iii-iv) GTCM remained unchanged under the same condition for one hour; (c) Optical retardance of CM and GTCM; and (d) The adhesion robustness measured as normalized critical pressure per membrane thickness of CM and GTCM and those treated with Pluronic (CM_Pluronic and GTCM_Pluronic). **(B)** Tuning CM porosity with nanoparticles (NP) as templates: (a) Schematics of the tuning process to form porous CM (pCM) by co-assembling NP in CM, crosslinking CM with GA and dissolving nanoparticles with dimethyl sulfoxide (DMSO); and (b) Membrane permeability characterized with FITC-labeled dextran (F-dextran) molecules of various size (4, 10, and 70 kDa), and the percentages of different F-dextran passed through the tested membranes. 4(A, B) are adapted with permission from The Royal Society of Chemistry [29, 39].

nanoparticles, resulting in porous CM (pCM). Next, permeability tests with FITC-dextran (F-dextran) molecules of different size revealed the enlargement in pore size of pCM in comparison with CM. Depicted in Figure 4B(b)-(i-iii) are fluorescent images of the CM and pCM made from different polystyrene nanoparticles size (25 and 200 nm), pCM25 and pCM200, taken in the permeability tests, while Figure 4B(b)-(iv) shows quantitatively the corresponding F-dextran passed through CM, pCM25, and pCM200 in terms of percentage. The results suggest that the procedure has successfully tuned the porosity of CM, as pCM shows improved permeability to macromolecules, confirming the capability to actively tune the CM's porosity as application demands.

Besides, the crystallize structures determined through optical retardance signals showed that GA treatment significantly influenced the crystallization of the flow-assembled CM in agreement with Hu et al. [39], while DMSO treatment induced little impact on the GTCM's microstructure [29]. The similar tendencies exhibited for pCM underwent the same treatment. The fact that no variation in optical retardance of the GTCM in treatment with DMSO was observed suggested that higher F-dextran transported across the pCM was not because of their altered microstructural organization. Instead, the variations in the mass transport of F-dextran of different size were probably induced by the difference in the interconnected pores instead of the membranes' crystallization [29]. Further investigations to confirm these hypotheses should be considered, and future studies to prove the practical usability of pCM in sorting a mixture of biomolecules are of interest. Furthermore, the concentration of incorporated nanoparticles is another key factor that determines the porosity of the fabricated pCM and further optimizations should be considered to attain the desired porosity and pore distribution for the fabricated membranes in the future.

4.3 Immobilization of bioactive reagents

One of the most important roles of chitosan in bioMEMS is to immobilize biomolecules, biological components, and other substances to microdevices. The abundant amine groups enable covalent attachment between chitosan and a variety of biomolecules and biological components, thus adding functionalities of microdevices for broader applications [24]. In this section, we summarize some of the modifications of the flow-assembled CM with biomolecules and other polymers (e.g., collagen) in microchips. Another exemplar of CM immobilized with mesoporous silica nanoparticles (MSNs) for personalized medicine applications is discussed in section 5.

In the first example, a carbon nanoparticle-chitosan (CN-CS) composite membrane was successfully fabricated in a microfluidic chip utilizing the flow-assembly technique for simultaneous adsorption and dialysis applications [7]. Depicted in Figure 5(a) is the fabrication process where the chitosan solution and buffer solution containing carbon nanoparticles (CN) were introduced to the microchip from the A and B inlets, corresponding. The polymerization reaction happened at the flow interface initiating the formation of the CN-CS membrane under various flow conditions. During membrane formation, the membrane was thinner in the upstream then thicker in the downstream, and the growth of the membrane was diffusion-limited, which resulted in uneven distribution of CNs inside the formed CN-CS membrane along with the flow interface. To improve this, CNs should be mixed with the chitosan solution instead of the buffer solution, which would result in a more uniform CN-CS membrane. Next, Figure 5(b) shows that the growth of the CN-CS membranes could be classified into two stages: (I) convection-driven growth (the membrane growth rate was fast, and the growth of the membrane was strongly affected by the convection transport of reactants along the flow direction); and (II) diffusion-driven growth (the membrane growth rate was slow, and the growth of the membrane was influenced by the diffusion transport of reactants across the formed membrane). Additionally, the authors observed that the growth rate and thickness of the CN-CS membrane were, in general, larger than those without CNs, as shown in Figure 5(c).

Furthermore, it is reported that as the flow rate increased, the CN-CS membrane's permeability initially rose, then reduced. This was explained because the longer the reaction time (which happened with the small flow rate), the more compact the membrane. However, as the flow rate increased, the reaction rate reduced, leading to a less compact membrane. Additionally, a porosity-correlated mass transfer model was used to theoretically simulate the urea transport across the fabricated CN-CS membrane and the approximate porosity of the membrane was determined by fitting the theoretical data to the experimental results. The pore size of the CN-CS membrane was roughly determined to be smaller than 3 nm. Lastly, with the addition of CNs, the formed CN-CS membrane exerted strong creatinine adsorption, while the creatinine adsorption of the blank CM was not significant as shown in Figure 5(d). Despite the promising results, it is important to note that the

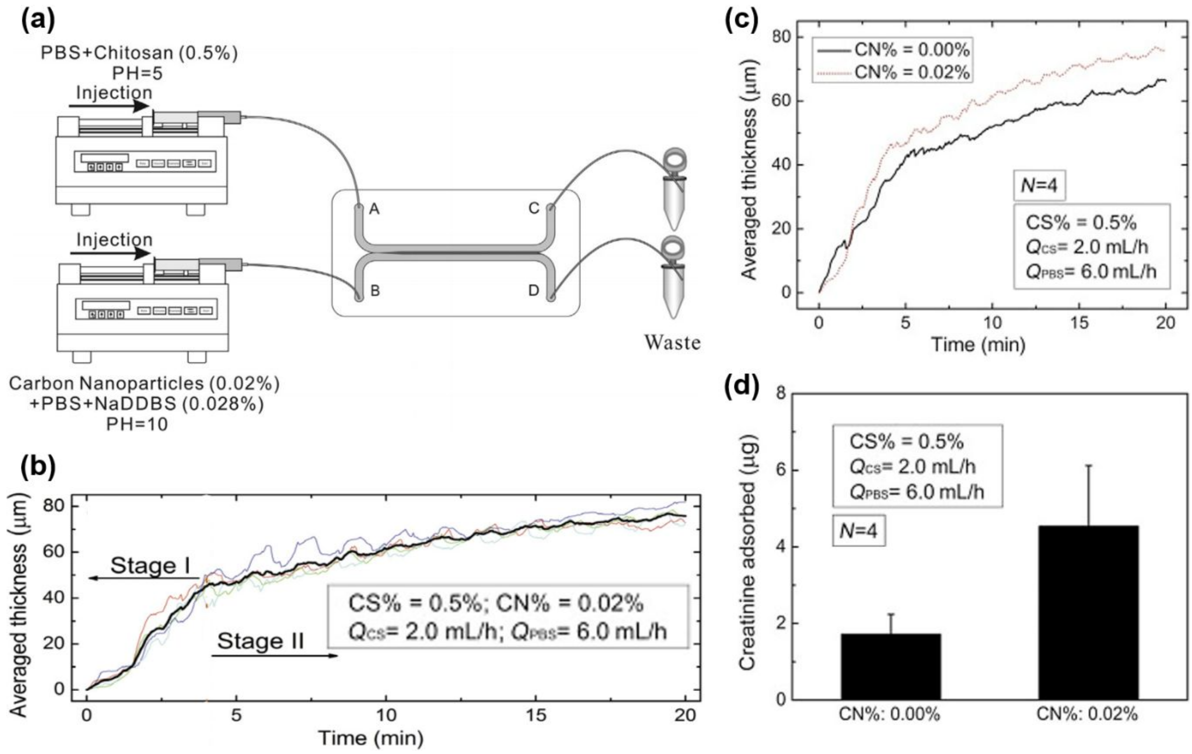

Figure 5: Fabrication of carbon nanoparticles-chitosan (CN-CS) composite membranes. (a) Schematic of the fabrication setup; (b) The averaged CN-CS membrane thickness over time. The black line is the average value of four repeated experiments; (c) Comparison of the growth curves with and without CN; and (d) Creatinine adsorption of the CN–CS composite membranes and the control (without CN). Adapted with permission from Elsevier [7, 55].

blood compatibility of the fabricated CN-CS membrane must be considered carefully and improved for future use of this membrane system as a micro-hemodialyzer [7].

The second example explored the immobilization of poly(N-isopropylacrylamide) (PNIPAM) nanogels to form a PNIPAM nanogel-containing CM in a microchip as generally depicted in Figure 6. Chitosan was used as a substrate material to embed PNIPAM nanogels to the membrane construct, enabling control over the fabricated membrane's permeability [30] through the reversible swelling/shrinking volume transitions correlated to variations in temperature [60, 61] and ethanol concentration (C_E) [62, 63] of PNIPAM nanogels. To construct such a desired membrane, a water phase solution comprising of chitosan and PNIPAM nanogels and an oil phase solution composed of terephthalaldehyde were introduced into two converging microchannels. The nanogel-containing CM was *in-situ* formed in microdevices through crosslinking reactions between chitosan and terephthalaldehyde instead of the localized pH gradient at the interface of the flow and trapped the PNIPAM nanogels inside the formed membrane construct. Figure 6A(a) shows the fabricated CM and nanogel-containing CM assembled by the interfacial crosslinking between chitosan and terephthalaldehyde. The embedded nanogels were tagged with red fluorescent dye to visualize their presence inside the membrane construct. Figure 6A(b-c) shows the blank CM and the nanogel-containing CM, in which the presence of PNIPAM nanogels in the crosslinked CM was confirmed with red fluorescence, which demonstrated that the flow-assembly of nanogel-containing CM in microdevices was a success [30].

The swelling and shrinking responses of the PNIPAM nanogels to the variations in temperature and C_E were characterized before being embedded into the membrane construct. The results revealed that as temperature increased from 25 to 40°C (volume phase transition temperature – VPTT), the mean diameter of the nanogels reduced significantly and the critical ethanol concentration (C_C) value was determined to be around 8%, above this point the nanogels experienced a significant decrease in size [30]. The nanogel contents in the fabricated membrane also played an important role in controlling its self-regulated permeability. As the nanogel concentration increased, the more dramatic temperature-responsive permeability control was attained, and the optimal nanogel concentration was determined to be 40 wt% [30]. Next, the self-regulated permeability of the fabricated nanogels containing CM in relation to temperature (Figure 6B(d)) and C_E (Figure 6B(e) changes in the microfluidic chip was examined with FITC. Briefly, at temperatures lower than the VPTT (T<VPTT), the nanogels in the membrane swelled and reduced the membrane's permeability to FITC (Figure 6B, a→b), while at temperatures higher than the VPTT (T>VPTT), the nanogels significantly shrank and increased the membrane's permeability to FITC (Figure 6B, b→a). Similarly, at 25°C, as the C_E became lower than the C_C ($C_E<C_C$), the nanogels swelled and reduced the membrane's permeability (Figure 6B, b→c), and whilst C_E was higher than the C_C ($C_E>C_C$), the nanogels significantly shrank and increased the membrane's permeability (Figure 6B, c→b). Most importantly, the authors confirmed that the volume transitions of the nanogels that enabled the self-regulation over the nanogel-containing membranes were reversible and repeatable. This enables a smart membrane platform for the development of micro-detectors, separators, sensors, or controlled release models. On the downside, this approach utilizes a crosslinking mechanism to enable such a membrane system [30], therefore, great care has to be taken to neutralize the residual crosslinker for biological applications.

Besides being the substrate to immobilize biomolecules to microdevices, chitosan can be modified with other polymers to enhance the physiochemical and biological properties for broader applications. Collagen is a commonly used material for a wide range of biomedical and tissue engineering applications thanks to its excellent biocompatibility, biodegradability, and non-

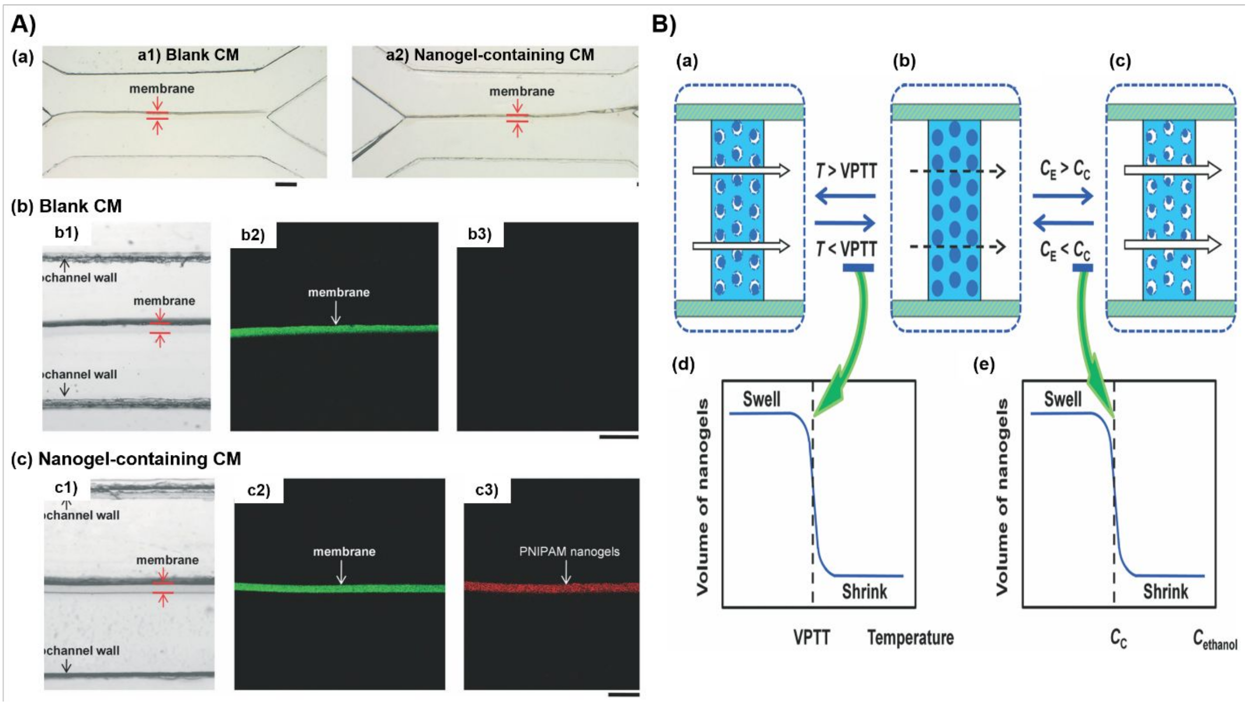

Figure 6: Fabrication of PNIPAM nanogels-containing CM. **(A)** Morphological characterization of the fabricated nanogel-containing CM: (a-c) Microscopic images of the (a1 and b) blank CM and (a2 and c) nanogel-containing CM (Scale bars: 250 µm). **(B)** Schematic illustrations representing the reversible swelling/shrinking transitions of PNIPAM nanogels in CM in response to changes in its volume-phase transition temperature (VPTT) and ethanol concentration (C_E), therefore controlling the permeability of nanogel-containing CM. Adapted with permission from The Royal Society of Chemistry [30].

immunogenicity [64-66]. However, the molecular alterations of collagen structure occurring during the extraction process generally results in a poor mechanical strength [67, 68]. Therefore, chitosan with excellent mechanical strength can serve as a support material for collagen-chitosan composite with enhanced biocompatibility inherited from collagen [69]. Rosella et al. reported a new microfluidic platform containing collagen-chitosan hybrid membrane and explored its role as an extracellular matrix (ECM) supports for biological applications [31]. Figure 7A(a) shows the illustrative design of the microfluidic system for membrane fabrication, in which four parallel experiments can be conducted simultaneously. Additionally, the impacts of flow rate on the hybrid membrane's growth rate were characterized. As shown in Figure 7A(b-c), the solution flow rates significantly affected the growth of the hybrid membranes, in which the thickness of the fabricated membranes significantly decreased as the flow rates were increased and the upstream membrane's thickness tended to be smaller than the downstream one. This was explained to be because the faster the flow rates, the shorter the fabrication time, and the narrower the pH gradient, ultimately, the thinner the membranes. Moreover, the faster flow rates induced higher shear forces at the surface of the formed membrane, leading to thinner and denser membranes as aforementioned [7, 31]. Further, polymer chains might also undergo repulsive interactions with the membrane surfaces under shear stresses, thus reducing the membrane's thickness [43, 44].

On the other hand, the biofabrication of a stable and highly aligned collagen matrix mimicking that in native tissue ECM is a long-standing design goal for biomedical and tissue engineering research [71-73]. To achieve this goal, Correa et al. demonstrated the fabrication of aligned collagen-alginate microgels through ionic crosslinking with divalent calcium ions. The fabrication process utilized CM as a barrier membrane to prevent the mixing of collagen-alginate co-polymer solution and calcium chloride solution pumped into two parallel microchannels, as schematically illustrated in Figure 7B(a). Then, calcium ions diffused through the cross-channel CM to interact with alginate in collagen-alginate solution and crosslink the copolymer into a hydrogel-like structure. Figure 7B(b) shows the fabricated collagen-alginate gels with different calcium concentrations formed within seconds as isolated islands in the single-aperture PDMS

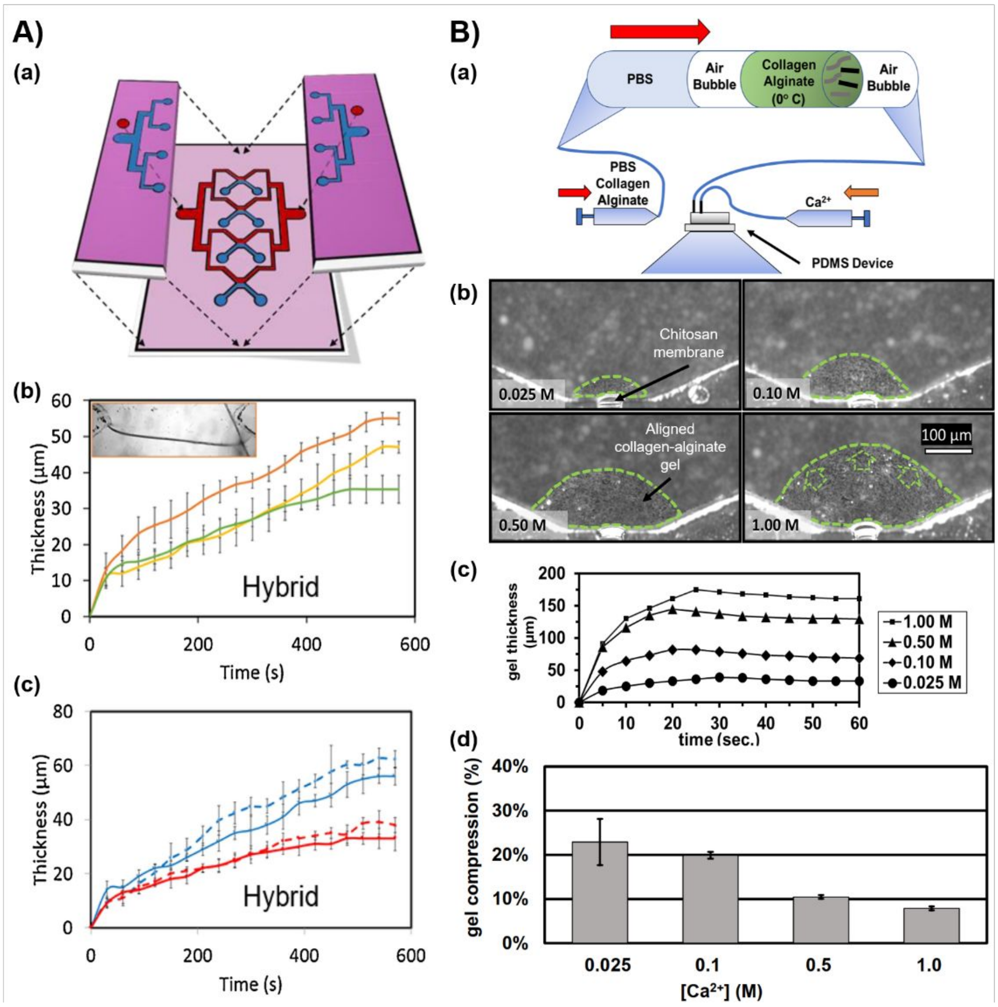

Figure 7: Fabrication of collagen-based matrices. **(A)** Fabrication of collagen-chitosan hybrid membranes: (a) Design of a parallel membrane synthesis system with 4 X-channels; (b) Formation of hybrid collagen-chitosan membrane for three total flow rates (Q_{total}): 1.03 (orange), 2.1 (yellow), and 5 mL/h (green); and (c) Width measurements of CM at the upstream (solid line) and downstream (dashed line) positions in the X-channel for fastest (red) and slowest (blue) flow rates used (b). **(B)** Fabrication of collagen microgels along with a CM in microfluidics: (a) Experimental setup to introduce collagen-alginate mixture and divalent calcium ions (Ca^{2+}) solutions into two parallel microchannels separated by a CM. Ca^{2+} diffusing across CM crosslink alginate and form an aligned collagen-alginate composite microgel adjacent to CM; (b) Images of aligned collagen-alginate microgels (green dashed) formed with different calcium concentrations (0.025, 0.1, 0.5, and 1.0 M); (c) The effects of calcium concentrations on collagen-based microgel thickness over time, and (d) its compression from peak thickness to steady-state thickness at 60 seconds after initial growth. 7A is adapted with permission from Elsevier [31]. 7B is adapted with permission from IOP Publishing [70].

devices. Figure 7B(c) shows the gel thickness characterization results, revealing that the gel thickness increased significantly with increased calcium concentration. It is also reported that the higher the calcium concentration, the lower the gel compression (Figure 7B(c)). Further, the aligned and stable collagen network was confirmed with the birefringence signal and circumferential texture orientation of the fabricated collagen-alginate microgels. Minor variations were observed in the dimensions of the fabricated gels after alginate was removed from the microgel structure. The collagen concentration of 8 mg/mL was determined to be the optimal concentration to form the most stable and asymmetric collagen microstructure matrix. The study reveals that the experimental parameters (co-polymer and calcium concentration, and solution flow rates) can affect the aligned and stable collagen gel formation in microfluidic devices. Such alignment approach by ions diffusion through CM enables gel formation with various microstructures, and can be valuable for lab-on-a-chip and tissue-on-a-chip applications [70]. Notably, the biofabrication of localized collagen gel for cell seeding along CM provides, for the first time, the spatiotemporal controllability with chemicals in flow that normally is only controllable with temperature, which can be further explored in important cellular studies and tissue engineering modelling.

5 Applications of flow-assembled chitosan membrane in microfluidic platforms

The flow-assembly of CM and CBM is a relatively new platform technology with many potentials to explore. In previous sections, we have presented the flow-assembled CM fabrication approach, recent advances in the flow-assembly of CM and CBM platforms, and the characteristics of the fabricated CM. This section is dedicated to reviewing the practical uses of CM-integrated microfluidic platforms for a variety of applications from biochemistry to biology to drug screening, including static gradient generator [35], platforms for shear-free cell culturing [31, 53], constructing synthetic ecosystems for cell-cell communication studies [36, 40, 74], and drug screening.

5.1 Static gradient generators

Chemical gradients occupy an essential role in directing cellular activities during chemotaxis, differentiation, inflammation, and many other biological processes [75-78]. Microfluidic-based gradient generators that enable highly controllable and quantifiable chemical gradients in a time- and cost-savings manner can be promising alternatives over conventional gradient generation models [79]. Compared to flow-based steady gradient generators, diffusion-based static gradient generators are more favorable for cellular studies thanks to their minimal convection and shear stress induced by laminar flows [80-82]. Chemical gradients can be readily established through diffusion-based transport along central microchannels connecting two side microchannels containing solutions of high concentration (source) and low concentration (sink). Various strategies have been developed to mitigate convective flow while enabling small molecules' diffusion to establish chemical gradients, thus, providing a convection-free culturing microenvironment. Luo et al. innovated a static gradient generator comprised of fourteen parallel CMs flow-assembled in a three-channel microfluidic device [35]. The middle microchannel acts as a static gradient chamber separated with the two side microchannels (correspond to the source and sink microchannels) by two parallel CM arrays that were 400 μm apart. The flow-assembly of parallel CMs were commenced with trapped air bubbles in the apertures, followed by membrane formation as previously reported [13]. The fabricated CM was uniform, strong, and semipermeable, which enables the diffusion of small molecules to establish the static gradients in the middle channel.

Figure 8A(a)-(i) illustrates the experimental setups to establish static gradients in the middle microchannel of the described above three-channel microfluidic devices. Briefly, FITC and PBS solutions were pumped into the source (left) and sink (right) side microchannels, respectively, while the central microchannel was filled with PBS and maintained in stop flow. Figure 8A(a)-(ii-iv) displays the evolution of static chemical gradients at 20, 60, and 600 seconds. The fluorescent intensity across the middle channel at a specific time point was measured and plotted in Figure 8A(b). It is clear that the chemical gradients evolved and an approximately linear static gradient was established after five minutes, and well-maintained after ten minutes [35]. Furthermore, this gradient generator was employed to establish the static gradient of α-factor to monitor the morphological change of yeast over time that is discussed in subsection 5.2. In the follow-up study, the porosity of fabricated CM was manipulated to enlarge the size of the pores, resulting in the pCM-based gradient generator that enabled the generation of macromolecule (F-dextran) gradients as similar to the FITC gradients established in the CM-based gradient generator [29]. This suggests that the proposed microfluidic-based gradient generator can be a facile and versatile platform technology for studies where static chemical gradient is desired.

It should be noted that even when there is no external flow, solute gradients can still generate steady convection by themselves due to the presence of buoyancy-driven and diffusioosmosis flows. Gu et al. adapted the above gradient generator containing *in situ* biofabricated parallel CM arrays to investigate the fluidic flows induced by steady solute gradients in relation to various system parameters including gradient magnitude, viscosity of fluid, microchannel dimensions, and solute type [52]. Figure 8B(a) shows a similar microfluidic design with W=400 μm, L=2 mm, and H=35-120 μm used in Gu et al. Upon applying different concentration solutions, c_1 and c_3, into the left- and right-side microchannels, respectively, the stable concentration gradient was established after ten minutes. The fluorescence intensity reduced linearly across the middle channel and the measured gradient was about 50% smaller than $(c_1-c_3)/W$ due to the resistance induced by CM (Figure 8B(b)). Through the modeling and experimental results, the authors suggested that some ways to minimize buoyancy-driven flows were to increase the solution's viscosity, reduce the channel's height to increase the viscous resistance to fluid motion, and decrease the difference in gravitational pressure. Furthermore, the buoyancy flows were reported to be temperature-dependent, in which such flows would be 30% larger at 37°C as compared to those that emerged at normal room temperature (22°C). Meanwhile, diffusioosmotic flows were independent of the channel's height and magnitude of the concentration difference but usually occurred in short microchannels derived from small concentration differences. To avoid such flows, it is better to employ concentration gradients where the magnitude of minimum concentration and maximum concentration was comparable. These system parameters should be designed carefully to mitigate the effects of buoyancy and diffusioosmotic flows for better quantification of cell chemotaxis and phoretic motions within colloidal [52]. It is worth to note that the solute gradient-induced convection is particularly true when the solute concentration and the gradient difference are in the high range of tens to hundreds of millimolar, in which steady flows several microns per second were predicted even within the small channels of microfluidic systems. Fortunately, cellular activities such as bacterial chemotaxis in reality are most apparent in the range of micromolar to a few millimolar [83-

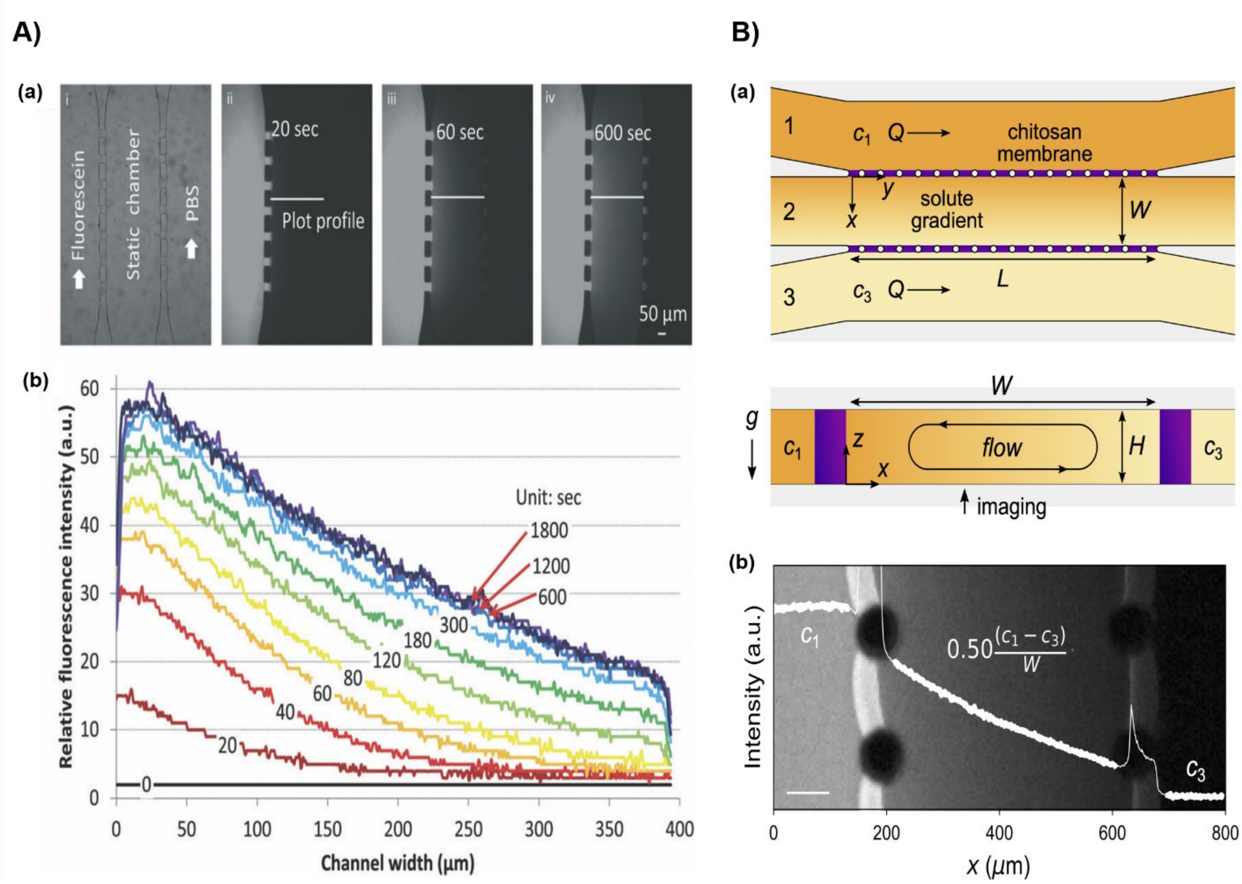

Figure 8: CM-integrated microfluidic platforms for biochemistry processes and analyses. **(A)** Generation of static gradient in a three-channel microfluidic device composed of parallel and semipermeable CM: (a)-(i) Experimental setups to generate a static gradient in the middle microchannel and (a)-(ii-iv) the established static gradients over time; and (b) Evolution of fluorescence gradients of the plot profiles indicated in (a) over time. **(B)** Measurement and mitigation of convection in CM-incorporated microfluidic gradient generator: (a) Schematic top-view (*xy* plane) of the three-channel microfluidic device and side-view (*xz* plane) of the solute-driven flows in the middle channel; and (b) Fluorescence image of the steady gradients across the center channel with a superimposed plot profile of the fluorescence intensity. Scale bar: 100 µm. Scale bar: 100 µm. 8(B, A) are adapted with permission from The Royal Society of Chemistry [35, 52].

[86]. Within this biological range, the buoyancy-driven and diffusioosmosis flows are minimal, and the gradients generated with parallel CM arrays in the three-channel networks can be fairly assumed to be static.

To conclude, microfluidic devices offer many advantages in generating concentration gradients for biochemical and cellular studies [87, 88]. For instance, microfluidic-based gradient generators can produce reproducible, predictable, and quantifiable gradients at low sample cost yet fast response time [88-90]. The described above static gradient generator comprised of parallel CM in three-channel PDMS device possesses many properties of a good gradient generator model. The platform fabrication process is rapid, facile, and robust, and the static gradients are quickly generated (within a few minutes) and stable over time in the static chamber [35]. However, when a high range of solute concentration and gradient difference is needed, several system parameters have to be taken into consideration to mitigate the buoyancy and diffusioosmotic flows as discussed above.

5.2 CM-based platforms for cell and tissue culture

Over the past two decades, integrated microfluidic platforms have been widely exploited for many biomedical and tissue engineering applications owing to their low reagent consumption, rapid fabrication, high sensitivity and controllability, and economical effectiveness [91]. These microfluidic platforms in combination with tissue engineering and cell biology have enabled the development of organ-on-a-chip systems. Several exemplar organ-on-a-chip systems include gut-on-a-chip [92], liver-on-a-chip [93], and lung-on-a-chip [94].

Using the flow-assembly platform technology, Rosella et al. developed microfluidic platforms consisting of biomembranes that acted as scaffolds closely resembling the native ECM for organ-on-a-chip applications [31]. In their study, three types of biomembranes were investigated including collagen, chitosan, and hybrid collagen-chitosan membranes. Moreover, CM and chitosan were used as a scaffold to support cell proliferation and substrate to enhance the mechanical strength of hybrid collagen-chitosan membranes, respectively. The system parameters (e.g. biopolymer type and solution flow rate) involved in the membrane fabrication process that affected the membrane's width, uniformity, and swelling ratio were well-characterized. The results showed that the properties of the fabricated membranes were flow-dependent, revealing an opportunity to customize and optimize the membrane's properties accordingly. Further, the cell biocompatibility of the fabricated biomembranes was tested with 3T3 fibroblast cells. The cells were injected and cultured in the corresponding biomembrane-integrated microfluidic platform for seven days and stained with live/dead assays. Figure 9A(a) shows the representative live/dead stained images of 3T3 fibroblasts at day 7 on collagen, chitosan, and hybrid collagen-chitosan membrane, respectively. As shown in Figure 9A(b), collagen membranes supported a significantly greater level of cell viability as compared to CM. Notably, there were no significant differences in cell viability among collagen and hybrid collagen-chitosan membranes. This suggested that the hybrid collagen-chitosan membranes possibly possessed not only great mechanical properties and processability of chitosan but also excellent biocompatibility of collagen, showing the potential for biological studies of such membrane systems [31].

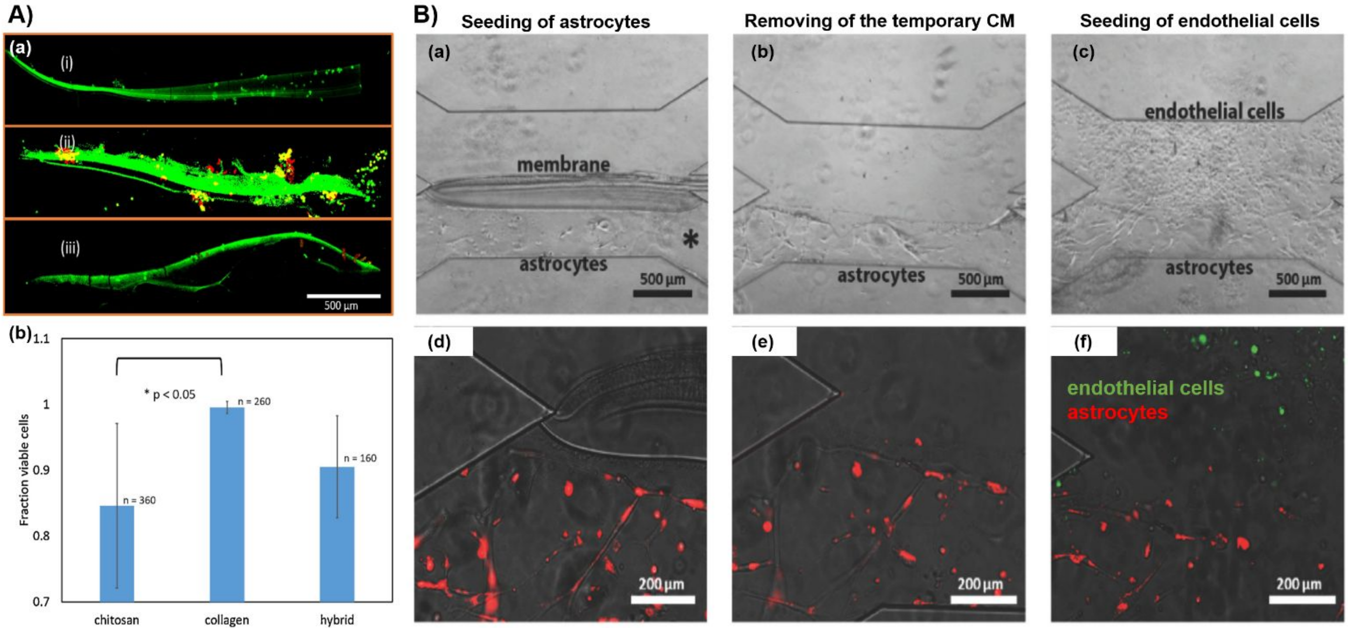

Figure 9: CM or CBM-integrated two-channel platforms for cellular studies. **(A)** Collagen-chitosan hybrid membranes for on-chip cell culture: (a) Live/dead (green/red) stained images of 3T3 fibroblast cells one week after being seeded on (i) collagen, (ii) chitosan, and (iii) collagen-chitosan hybrid membranes; and (b) Cell viability for each membrane type (* indicates $p<0.05$ using one-way ANOVA analysis, n = 4). **(B)** Temporary CBM for organ-on-chip applications: (a, d) Astrocytes are homogeneously distributed within the extracellular matrix-like gel (Matrigel) in one channel marked with an asterisk (*); (b, e) 18 h after seeding the astrocytes, the temporary CM is completely removed using acetic acid (pH=5.0). The morphology of the astrocytes is not influenced by the removal of the CM; (c, f) Subsequently, the channel is coated with a fibronectin solution, followed by the seeding of brain-endothelial cells in the empty channel. The endothelial cells reach almost 100% confluence after 24 h. 9A is adapted with permission from Elsevier [31]. 9B is adapted with permission from Wiley [53].

Another exemplar of CM use in the organ-on-a-chip field is the ability to be removed with a mild acidic solution to enable a direct cell-cell interface. Previously, it was challenging to recreate a native interface between parenchymal and vascular endothelium tissues in blood-brain barrier microfluidic models. While commercial polymer membranes might not mimic the stiffness, porosity, and interconnected porous structure of the native basement membrane, the utilization of CM as the temporary membrane could create direct contact between two tissue types, thus enabling the coculture of multiple cell types in the absence of synthetic membrane [53]. Figure 9B shows the overall experimental process. Initially, the CM was flow-assembled at the interface between the acidic chitosan and the basic buffer solutions as described above. Next, human astrocytes in Matrigel were seeded and cultured for one day at the bottom microchannel (Figure 9B(a, d)), followed by the removal of CM using the mild acidic solution (Figure 9B(b, e)). Subsequently, the other microchannel was coated with a fibronectin solution prior to the seeding of brain endothelial cells, resulting in a human astrocytes-brain endothelial cells coculture that allowed for direct cell-cell interaction of the two cell types inside the microfluidic chip (Figure 9B(c, f)). Thus, the proposed membrane fabrication and removal process can be employed to produce membrane-free cocultures in microdevices for broader organs-on-a-chip applications. Perfusion with flow for long-term culturing is yet to be integrated. For future studies, the possible cross-invasion of both cell types over long-term culture without the barrier membrane is worth investigating.

5.3 CM-based platforms for cellular signalling studies

Besides the mammalian cell culture applications, CM-integrated microfluidic platforms have been demonstrated to be useful for a variety of bacterial chemotropism and bacterial cell-cell signalling studies [95, 96]. For instance, the ability to generate static gradients within the middle microchannel of a three-channel microfluidic platform containing parallel CM is utilized to study the evolution of morphological change in yeast under matting pheromone α-factor gradients over time [35], and to monitor the chemotropism between adjacent populations of multiple yeast types [42].

For the first application, it was reported that the target strain of yeast would react to the matting pheromone α-factor and change to elongated shmoo-shaped yeasts with the tips intrinsically grown towards to source of α-factor. Upon applying the growth media (YPD) containing *in vitro* α-factor and normal YPD solutions to the source and sink microchannels, respectively as depicted in Figure 10A(a), no obvious yeast morphology change was noted during the first 100 minutes. Then the yeast started to grow into elongated shapes and stopped dividing after three hours. Figure 10A(b, d, e) shows the zoom-in images of the middle microchannel where the morphology of the yeasts presented a gradient-dependent transition in aspect ratio (length ratio of long axis to short axis). The gradient-dependent transition was well-distinguished within the middle microchannel where more yeasts were elongated from the source (right) towards the sink (left) side microchannel. Figure 10A(f) shows the quantification of the average aspect ratio of the yeasts over time in the five separate blocks, as indicated in Figure 10A(c). A gradient of an increasing aspect ratio of the yeasts was observed across the middle microchannel from the source to the sink side microchannels over time. Thus, the flow-assembly of CM provides a rapid and facile platform technology for static gradient generation studies and is promising for many biology studies where convection-free static gradients are vital [35].

Numerous microfluidic platforms have been developed to monitor chemotropic responses of cells in relation to the *in vitro* generated chemical gradients of synthetic matting peptides, and to provide new insights for a better understanding of chemotropism in multiple cell types [97-101]. Nevertheless, the chemotropic response of cells to *in vivo* chemical gradients is dynamic and cannot be closely modeled with synthetic matting pheromones. Additionally, cells in

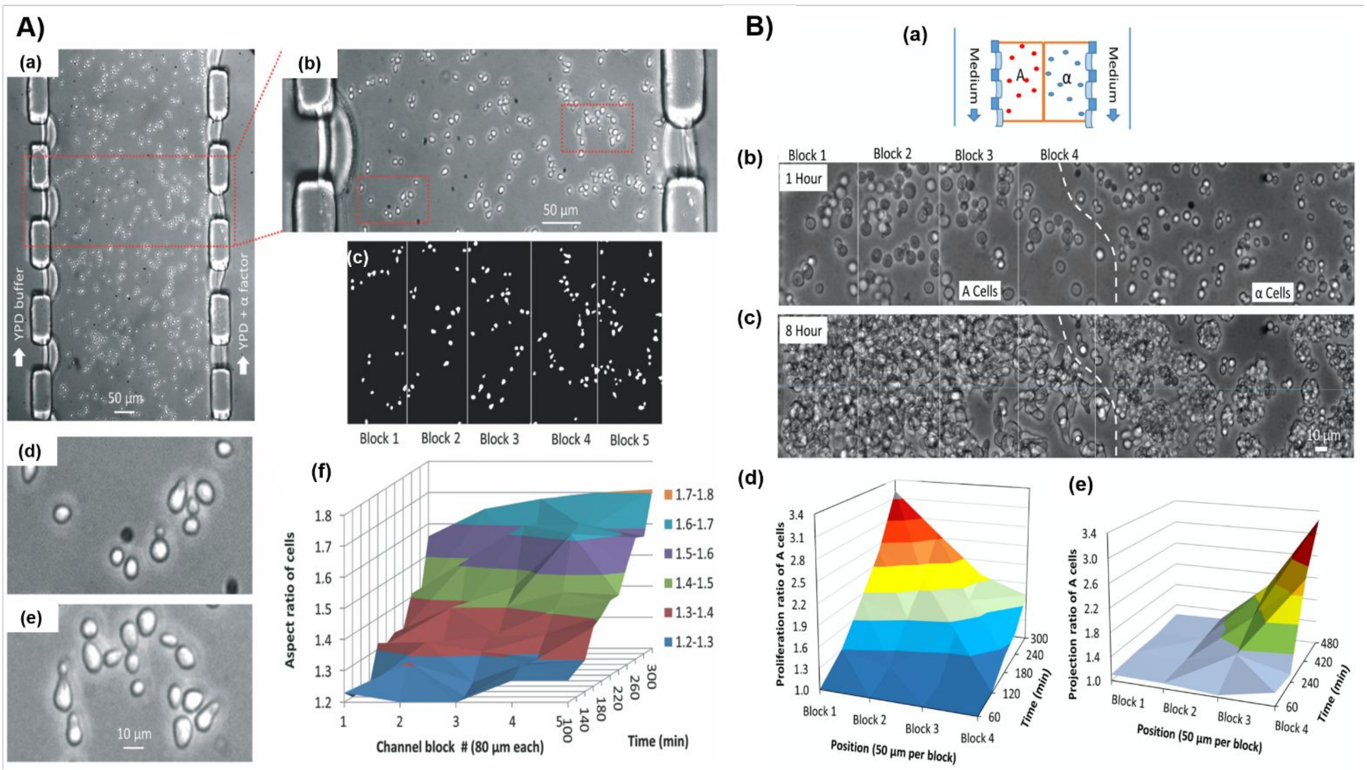

Figure 10: CM-integrated three-channel platforms for cellular studies. **(A)** Monitoring morphological changes of yeasts in response to static gradients of *in vitro* alpha factor (α-factor): (a) Yeast cells in middle microchannel were exposed to the static gradients of α-factor with continuous flows of growth media (YPD) and α-factor in YPD in the sink (left) and source (right) side microchannels, respectively; (b) Zoom-in image of the red rectangle in (a); (c) Morphology of yeasts in the five separated blocks to quantify the average aspect ratio; (d, e) Zoom-in shmoo shapes of yeasts in the left and right red rectangle in (b), respectively; and (f) Average aspect ratio of yeasts in the five separate blocks over time. **(B)** Monitoring *in vivo* chemotropism between adjacent populations of yeasts: (a) Schematic of the A- and α-yeasts assembled side-by-side in the alginate hydrogel assembled in the middle microchannel of a three-channel microfluidic device; (b) Relative uniform distribution of A- and α-yeasts one hour after assembly; (c) Distribution and morphologies of A- and α-yeasts eight hours after assembly; (d) Proliferation ratio of A-yeasts in the four indicated blocks in (b, c); and (e) Projection ratio of A-yeasts in the same four blocks. (c-e) Together shows the chemotropism of A-yeasts closer to α-yeasts as compared to continuous proliferation of A-yeasts away from α-yeasts. 10A is adapted with permission from The Royal Society of Chemistry [35]. 10B is adapted with permission from Biomicrofluidics [42].

nature tend to be heterogeneous, which may affect the chemotropic responses or the established chemical gradients. Vo et al. proposed a CM-based microfluidic platform that contains populations of multiple yeast strains, the mating A- and α-yeasts, to monitor their mutually chemotropic responses with spatiotemporal programmability and sensitivity. Figure 10B(a) shows the schematics of A- and α-yeasts positioned side-by-side in alginate hydrogels in the previously developed three-channel microfluidic platform containing parallel CM arrays to allow nutrient diffusion from the side microchannels. The strain A of yeast was positioned at the left-handed side separated from the α-yeasts at the right-handed side, where the yeast distribution was relatively even after one hour (Figure 10B(b)). After eight hours, A-yeasts in blocks 1 and 2 that were far from α-yeasts continued to grow while those in proximity with α-yeasts formed shmoo structures and underwent cell cycle arrest, indicating the mating response to *in vivo* pheromone gradients (Figure 10B(c)). Furthermore, Figure 10B(c) also shows that the proliferation of α-yeasts was independent of the closeness to A-yeasts.

Quantitatively, Figure 10B(d) shows a gradual decrease in proliferation ratios of the A-yeasts from block 1 to 4 over the first five hours, indicating that the pheromone secreted by the α-yeasts had initiated the mating responses and induced cell proliferation of A-yeasts. In contrast, the projection ratios increased steadily from block 1 to 4, illustrating the chemotropic responses of the A-yeasts towards the pheromone emitted from the α-yeasts and induced morphological changes (Figure 10B(e)). These suggested that the chemotropic responses of A-yeasts in relation to a mating pheromone secreted from α-yeasts were spatially dependent, while α-yeasts were not as sensitive to A-factor as A-yeasts to α-factor. Furthermore, the authors reported that the chemotropic responses of A-yeasts were dependent on cell density, with individual A-yeasts developing into shmoo shapes tending to direct more precisely toward the α-yeasts. Meanwhile, a cluster of A-yeasts received less pheromones from α-yeasts and tended to proliferate more except that those around the edge of the clustered could sense pheromone better, therefore, shifted from proliferation to cell cycle arrest and shmoo formation. Lastly, the direction of shmoo projection of the A-yeasts was concentration-dependent in microscale-spatial resolution. In sum, the work demonstrated that the CM-based microfluidic platform could be utilized to assemble and investigate population-scale, spatial-sensitive cell-cell signalling behaviors similar to *in vivo* and chemotropism between multiple cell types [42].

5.4 Biofabricated synthetic ecosystems

Further, communications between multiple cell types in a complex heterogeneous microenvironment not only direct their biological phenotypes but also reassemble the synthetic environments of native ecosystems spanning different length scale. To enable such communications, Luo et al. presented an approach to biofabricate multiple populations of cells in microfluidic devices with spatiotemporal programmability [36]. As schematically illustrated in Figure 11A(b), the authors utilized the permeability of CM that allowed Ca^{2+} ions to diffuse from one microchannel through the membrane and interact with alginate containing cell solution on the other side. The Ca^{2+} would ionically crosslink carboxylate groups on the guluronic acid residue of alginate to biofabricate a three-dimensional cell-gel composite (Figure 11A(a, b)). The thickness of the formed cell-gel composite could be controlled with the diffusion time of Ca^{2+} via the CM or the concentration of Ca^{2+}, then the un-crosslinked alginate solution would simply be rinsed with deionized water. The proposed biofabrication of multiple cell types in microdevices provides a facile, rapid, and versatile platform system for *in vivo* cell-cell communications in the modelled heterogeneous microenvironment studies. The semipermeable CM not only provides a barrier between two cell populations but also acts as a supporting backbone for the alginate hydrogels. Furthermore, this platform system allows for independent fluidic access to each cell layer and manipulations over generated biological signalling by varying the system parameters such as the fluidic flows inside the microchannels [36]. It is also possible to assemble multiple layers of alginate hydrogels containing multiple cell types in various configurations as shown in Figure 11A(c). Thanks to the spatiotemporal programmability in assembling cell populations in the microenvironmental length scale of biological relevance, such platform systems were used to innovate synthetic ecosystems for biological applications.

First, a platform system consisting of two adjacent cell populations of transmitting and reporting cells separated by CM in between was developed, which allowed for direct observation and manipulation of autoinducer-2 (AI-2) quorum sensing (QS) signalling [36]. Figure 11B(a) schematically depicts the assembly of transmitting and reporting cells containing alginate hydrogels in microchannels B and A, respectively. Briefly, the transmitting cells simultaneously secreted AI-2 signalling molecules and constitutively expressed GFP for direct observation. The reporting cells then sensed the secreted AI-2 and instantaneously produced DsRed, evidence of QS response [102] and an example for many AI-2 induced behaviors [103]. It was reported that during the first five hours of culturing, the cell density of both strains (transmitting and reporting cells) increased rapidly and started to leak out of the alginate hydrogels at around the 5th hour. As seen from Figure 11B(b-d), after the first five hours, the AI-2 concentration secreted by transmitting cells reached the adequate amount that the reporting cells sensed and expressed the QS responses by emitting DsRed and reached a plateau after 11 hours. In the representative case of 0.05 μL/min flow rate in the reporting channel shown in Figure 11B(b), a gradient of QS response from the upstream flow to downstream was observed at the 5th and 8th hour time points. This was explained due to the shear stress applied on the upstream channel that carried away the AI-2 and delayed the QS behaviors of the upstream reporting cells. By varying the flow rate of nutrients supplied in microchannel A and stopping the flow in the microchannel B, the authors observed a significant trend that as the flow rate increased, the DsRed reduced dramatically. Particularly, the DsRed fluorescence intensity increased steadily at the flow rate of 0.05, 0.1, and 0.2 μL/min, while that remained relatively low at the flow rate of 0.3 and 0.4 μL/min (Figure 11B(d)). This suggested that the AI-2 level in the case of high flow rates (0.3 and 0.4 μL/min) never reached the adequate amount, since the high flow rate continuously diluted or created high shear forces throughout the microchannel and disposed of the AI-2 secreted by the transmitting cells. The results demonstrated that QS responses in the stratified biofilms could be simulated and manipulated by adjusting the flow conditions using the proposed platform technology that allowed for cell-cell interaction studies and small molecule drug discovery [36].

Another notable application of CM-integrated microfluidic systems is the modulation of *E. coli* cell-cell signalling in close and distal proximity [74]. The developed microfluidic system consisted of two individual microdevices that were connected by flexible tubing to transmit AI-2 signalling molecules, which were produced by the transmitting cells residing in the upstream device, to the modulating cells, which either amplified (enhancer) or attenuated (reducer) the signals, before transmitting to the reporting cells. Both the modulating and reporting cells were in the downstream device (Figure 11C(a-c)). Such a microfluidic system allowed for the modulation of longitudinal transport of small molecules produced by *E. coli* that closely resembled distant signalling pathways observed in the human intestinal tract [74, 95]. The results reported that the molecular signals could be transmitted from the transmitting to the reporting cells located at a long commuting distance. Figure 11C(d) shows the growth rate of reporting cells in optical density (left axis) and fluorescence intensity (right axis). Overall, the reporting cells grew consistently over time, and it took approximately two hours for signal transport and four hours for QS responses. There were significant differences in fluorescence intensity among different configurations, in which the fluorescence intensity was the highest when the reporting cells were assembled with an enhancer (red), followed by that with a clear alginate hydrogel (control, yellow). Meanwhile, the fluorescence intensity of the reporting cells assembled alongside with the reducer dropped tremendously (blue) and was at the lowest with two reducers (black). Furthermore, the concentration of AI-2 available for reporting cells in various configurations (assembled with enhancer, control, and reducer) was also approximated using numerical simulation that showed a strong agreement with the real-time fluorescence intensity from the reporting cells (Figure 11C(e)). Hence, the reported microfluidic system reassembles a synthetic ecosystem mimicking the human gastrointestinal tract, and can be applied for various cell populations such as epithelial cells and manipulating effector molecules (glucose, hormones, ions) with spatiotemporal control [74].

Despite the promising applications of such biofabricated platforms in monitoring QS responses in close and distal proximity, several problems remain to be solved. First, the mechanical strength of alginate hydrogels is relatively weak that can easily be delaminated from the PDMS device under strong laminar flows [36]. This requires that the length and thickness of the assembled alginate hydrogels have to reach a certain size to be able to withstand shear forces and secure their location within microfluidic channels. Second, the shear stress induced by laminar flows can remove the signaling molecules, resulting in the transient gradient of QS responses as observed in Figure 11B(b). Furthermore, the alginate hydrogels can be degraded quickly without the continuous supply of Ca^{2+}, thus, leading to an unwanted mixing of multiple cell populations. To avoid this scenario, the growth media is usually supplied with a low concentration of Ca^{2+}. This, however, produces a new problem as Ca^{2+} is a sensory ion for gene expression of biofilm-associated growth and can alter bacterial adhesion and biofilm formation [104-106], therefore it may influence the experimental results.

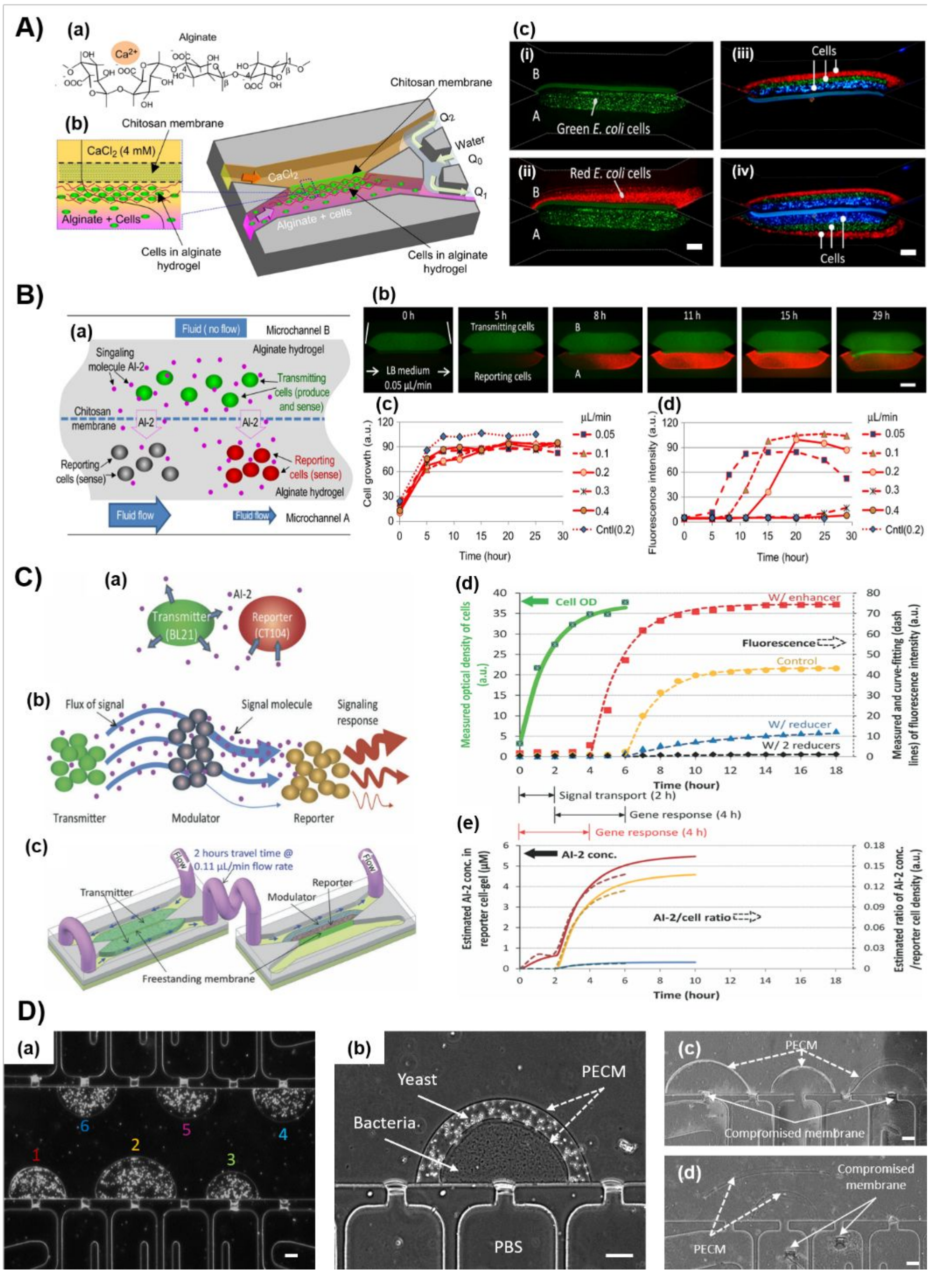

Figure 11: CM-integrated platforms as synthetic ecosystems for cell-cell signaling studies. **(A)** CM-facilitated assembly of multiple cell populations: (a) Alginate molecular structure chelated with Ca^{2+}; (b) Assembling cells in alginate hydrogel with Ca^{2+} diffusing through CM; and (c) Various configurations to assemble multiple cell populations in alginate hydrogels: (i) Two CM enclosing one *E. coli* population (green), (ii) one middle CM sandwiched by two *E. coli* populations (red & green); (iii) three layers of *E. coli* populations (blue, green, and red) sequentially assembled on one side of CM then (iv) on the other side of a middle CM. Scale bars: 200 µm. **(B)** Stratified biofilm mimics for observing and controlling bacterial signaling: (a) Schematic of flow dynamics impacting on multicellularity signaling between *E. coli* transmitting and reporting cells separated by a middle CM. Bacteria were cultured with flows at 0.05, 0.1, 0.2, 0.2 (control), 0.3 or 0.4 µL/min flow rate in channel A and no flow in channel B. (b) Representative fluorescence images of the transmitting and reporting cells for the case of 0.05 µL/min flow rate; (c) The growth of reporting cells over time; and (d) Fluorescence intensity of reporting cells over time with deferred (0.1 and 0.2 µL/min), extinguished (0.3 and 0.4 µL/min) or no (control at 0.2 µL/min) DsRed protein production with increasing flow rates. **(C)** Modulation of distal cell–cell signaling: (a) Schematic of quorum sensing (QS) between transmitting and reporting cells; (b) Schematic signaling flux from transmitter to reporter cells either enhanced or reduced by modulator cells; (c) Schematic of distally connected cell–gel composites in two microchannels; (d) Typical cell optical density (OD) (left axis) and fluorescence intensity of the reporter cells (right axis) over time showing various signaling modulation effects; and (e) Estimated AI-2 concentration within the reporter cell–gel composites (left axis, solid) and estimated AI-2 concentration per cell OD (right axis, dotted). **(D)** Inter-kingdom synthetic ecosystems: (a) Assembly of six separate yeast cell populations (labeled 1 to 6) along with the CM (referred to as fluitrodes in the study) by alternatively introducing yeast-alginate mixture solution, crosslinking with Ca^{2+}, rinsing with PBS, followed by enclosing with a protective PECM layer; (b) Multilayered bacteria and yeast separated by PECM on one single fluitrode; and (c, d) Extraction of bacteria and/or yeast with vacuuming for downstream analyses using Pluronic treatment to compromise CM. Scale bars: 50 µm. 11(A, B) are adapted with permission from ScienceDirect [36]. 11C is adapted with permission from The Royal Society of Chemistry [74]. 11D is adapted with permission from Wiley [40].

Pham et al. developed a new microfluidic platform consisting of 12 individually addressable CM, referred to as fluitrodes, to enable the programmable assembly of multiple cell populations in alginate hydrogels in the length scale of biological relevance (Figure 11D(a)). The concept of individually addressable fluitrodes allowed the separate delivery of nutrients and signaling molecules, enabled the assembly of more cell populations (up to 12 different cell species) in one single device, and facilitated the release of embedded cells for further bioassays and molecular analyses [40]. Specifically, six alginate hydrogels containing yeasts of the same strain were sequentially assembled on six individually addressable fluitrodes with the biofabrication process described above and in the previous publication [40]. To protect the assembled alginate hydrogels and prevent leakage of cells, the authors enclosed the six microbial constructs with PECM, as illustrated in Figure 11D(a), by allowing chitosan to interact with alginate hydrogels. The enclosure of PECM also significantly improved the mechanical robustness of the assembled alginate hydrogels under a strong laminar flow rate of around 1250 µL/min. Next, it was demonstrated that multiple species of cell populations could be assembled side-by-side on one single fluitrode, enabling the monitor of different species' responses to the same type of nutrients or signaling molecules in juxtaposition. The side-by-side alginate hydrogels were also separated by PECM in between to prevent the unwanted mixing of different cell types (Figure 11D(b)). Lastly, this fluitrode platform allowed for the sequential release of embedded cells for downstream analyses. For this purpose, the CM was compromised and detached from the apertures using Pluronic F-127, enabling the sequential extraction of embedded cells (from both separate yeast populations and multilayers of yeast and bacterial cells) by vacuum pressure as shown in Figure 11D(c, d). No significant effect, however, was observed on the viability of bacteria embedded in the CM-supported alginate hydrogel and maintained at physiological conditions despite chitosan being a prominent antibacterial and antifungal agent. This agrees with previous studies that reported no inhibitory effects of chitosan/alginate composites on bacterial growth [107, 108]. The main reason for this can be due to the mode of inhibitory action of positively charged chitosan. Similar to the antibacterial mechanism of metallic nanoparticles [21, 109, 110], amino groups carrying positively charged of chitosan can easily attract and penetrate to negatively charged cell membrane of bacteria, then disrupt respiratory process and cause bacterial death [111, 112]. Therefore, the culture environment should be maintained at physiological pH to prevent the protonation of amino groups that may affect bacterial viability and intervene experimental results.

In summary, the developed fluitrode platform provides real-time observation of *in vitro* synthetic ecosystems for cell-cell communication in their complex heterogeneous microenvironment, and can broaden the applications of CM-integrated microfluidic platform in high throughput drug screening [40]. Furthermore, this study addressed some of the challenges experienced in previous works with the addition of PECM to protect and secure the assembled alginate containing cells in hydrogels in the absence of extra Ca^{2+}, and to prevent the mixing of different cell types.

5.5 Drug delivery

Drug delivery systems and drug screening are among the most important applications of microfluidic platforms. The superior advantages of low sample consumption, fast reaction time, cost-saving, high throughput, and reproducibility can aid in the development of new drugs and strategies for efficient drug delivery [11, 113, 114]. Jia et al. have explored the CBM-integrated microfluidic platform to program complex release of nanocarriers [37].

Mesoporous silica nanoparticles (MSNs) are a nanoparticle-based drug delivery system that has gained significant research interest thanks to their high surface areas, large pore volume, and tuneable porosity that can protect therapeutic agents for controlled and targeted drug delivery. The controlled release of MSNs is based on a variety of physical, chemical, and biological stimuli [115, 116]. However, the controlled release based on the pH-responsiveness of MSNs usually requires complicated chemical grafting methods that can result in pore blockage or toxicity issues [117]. Jia and colleagues proposed, for the first time, a pH-responsive CM containing MSNs for drug delivery in microfluidics [37].

Figure 12(a) illustrates the schematic design of the microfluidic device with multiple upstream microchannels for rapid changing of different chitosan containing MSNs, base, and PBS solutions, allowing for the synthesis of multi-layered CM containing MSNs. For instance, a bilayer CM containing positive MSNs with FITC-tag ($\boldsymbol{MSN_F^+}$, green) and those with rhodamine B-tag ($\boldsymbol{MSN_R^+}$, red) was assembled at the flow interface as shown in Figure 12(b). Different types of MSNs embedded in layer-by-layer CM remained unmixed over the tested time frame (4 hours). Next, the release of the embedded MSNs using a mild acidic solution (pH=5.0) over time was demonstrated in Figure 12(c). A gradual decrease in membrane thickness and subsequent release of the embedded MSNs was observed within the first ten minutes and completely dissolved after 15 minutes with the erosion rate to be around 480 µm/h. To enable the delayed dosing and sustained drug release, the authors developed two-MSN-capped CM separated by a pure CM as depicted in Figure 12(d)-(i). The release profile of such a membrane system in acidic solution (pH=5.9) could be prolonged for up to two hours as shown in Figure 12(d)-(ii). Lastly, a complex 7-layer CM capped MSNs was also assembled by flows with the release profile in acidic solution (pH=5.9) that lasted for up to four hours (Figure 12(e)). Hence, by accurately manipulating the precursor solution flow rates for highly programmable membrane formation, MSNs-embedded CM with complex layered architectures for customizable drug release was successfully presented. The presented flow-assembled CBM-based platform for complex release profiles of embedded therapeutic agents is attractive and can be applied for a wide range of biomedical applications and personalized therapy [31]. Importantly, the release profile of CM-embedded therapeutic agents can be easily manipulated by treating the membrane with crosslinking agents.

6 Conclusions and future perspectives

Chitosan has been demonstrated as a valuable material for broad biological functionalization in bioMEMS. Utilizing laminar flows to deposit freestanding CM inside microfluidic networks is a rapid, facile, and versatile approach to integrate biology (or biological materials) with inorganic microdevices. Furthermore, the ability of *in situ fabricating* freestanding biopolymer membranes inside microchannels not only overcomes the unwanted leakage, insufficient sealing, complex and expensive fabrication process but also enhances the biological friendliness of integrated bioMEMS. In this section, we summarize the key ideas that this review aims to convey and disclose some possible directions for future studies.

First, by creating the localized pH gradient, the freestanding, robust, well-aligned, and semipermeable CM can be readily formed at the interface of the converging flows of the chitosan solution and a countering basic buffer or alginate solution in a spatiotemporally controlled manner. While the use of a basic buffer solution requires a stable flow interface achieved through precise pressure-balancing, the other tactic enables the facile formation of CM on PECM generated upon the spontaneous contact between chitosan and alginate macromolecules. The addition of PECM to the flow-assembly of CM significantly enhances the capability to immobilize a wide variety of biomolecules or biological components thanks to the presence of both amine and carboxyl functional groups. Further, the PECM aids to stabilize and separate the subsequently biofabricated synthetic ecosystems of multispecies entrapped in alginate hydrogels, providing closely resembled microenvironments for cell-cell communication/signaling studies [40, 42]. Besides basic buffer and alginate solution, crosslinking agents such as glutaraldehyde [29, 39], terephthalaldehyde [118, 119], and tripolyphosphate [120, 121] can be explored in the flow assembly of CM in microfluidics.

To enhance the reliability of the fabrication process, our group developed two improvement strategies: one is to include an extra downstream acidic input in the device design to rinse any undesired residue deposition [36], the other is to use an add-on vacuum layer that can dissipate air bubbles trapped in apertures through the gas-permeable PDMS layer [41]. Meanwhile, other groups design microchips with circular pillars and precise pumping to skip the formation of air bubbles [44], or include an extra outlet to act as an anchoring point for the membranes [53]. On the other hand, the solubility in slightly acidic solutions and low-molecular weight cut-off of the flow-assembled CM (only a few nanometers) might limit the applications of their integrated microfluidic platforms. To overcome those problems, several works have been conducted to modify the properties of CM for broader applications [29, 39]. Additionally, many bioactive materials including PNIPAM nanogels [30], carbon nanoparticles [7], or collagen [31] have been successfully immobilized in microfluidics utilizing chitosan as an embedded substrate to enhance the functionality and applicability of the fabricated integrated microfluidic platforms.

Since the first invention in 2010, flow-assembly of CM has gained more and more attention from scientific communities as a promising platform technology. The flow-assembled CM-integrated microfluidic platforms have been widely exploited in a variety of important biochemical and biological applications, which include static gradient generator [35], platforms for shear-free cell culturing [31, 53], and synthetic ecosystems for cell-cell communication studies [36, 40, 74]. Additionally, multi-layered CM has recently been developed to investigate complex release profiles of mesoporous silica nanoparticles for personalized medicine applications [37]. Last but not least, the

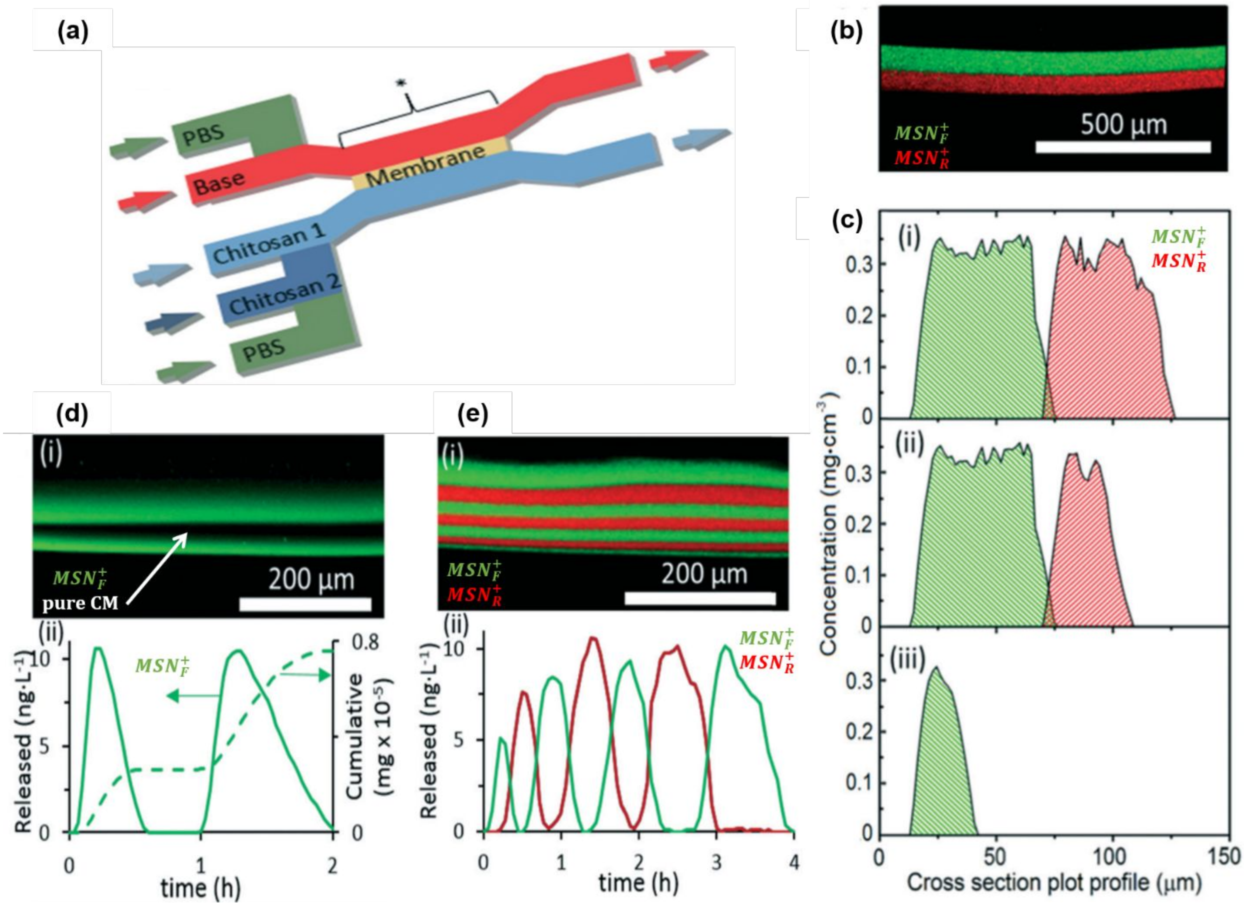

Figure 12: CM-integrated microfluidic platform for complex release profiles of nanocarriers: (a) Schematic of the X-channel showing the inlets of basic (red), chitosan (light & dark blue), and PBS solutions for step-wise control over the flow-assembly of the membrane (yellow) at the aperture; (b) Fluorescence image of a bilayer CM containing positively charged mesoporous silica nanoparticles (MSN^+) with FITC-tag (MSN_F^+) and with rhodamine B-tag (MSN_R^+), respectively; (c) Cross-section profiles during membrane dissolution at (i) 0 min, (ii) 4 min and (iii) 10 min after pH of 5.0 solution was introduced to the bottom channel at 1.0 mL/h; (d)-(i) Fluorescence image of 3-layer CM with the first and third layers containing MSN_F^+; (d)-(ii) Normalized instantaneous (solid) and cumulative (dashed) MSN_F^+ release profiles during dissolution; (e)-(i) Fluorescence image of 7-layer CM with MSN_F^+ (green) in layers 1, 3, 5, and 7, with MSN_R^+ (red) in layers 2, 4, and 6; (e)-(ii) instantaneous MSN release profiles during dissolution. A pH=5.9 solution was introduced to the bottom membrane side at 1.0 mL/h for dissolution in (d)-(ii) and (e)-(ii). Adapted with permission from The Royal Society of Chemistry [37].

horizontal layout of the CM- and CBM-integrated microfluidic platform not only allows direct visualization of cellular interactions and high-resolution live imaging but also enables a simpler quantification process as compared to existing sandwiched platforms [35, 40, 122].

The current review reports the recent progress in the flow assembly of CM in microfluidics and the implementations of this promising platform technology that provide insights and open many opportunities for future research and application. First, future studies can focus on developing feasible characterization approaches since the physiochemical properties of CM and CBM remain difficult to be investigated due to the tiny size of these membranes and intrinsic enclosure nature of microdevices. Second, more works can be done to immobilize biomolecules and biological entities to chitosan and/or alginate backbones, in case PECM is present, for broader applications. For example, the biofabrication of three-dimensional hydrogel microenvironments with embedded cells using the semipermeable CM as an architecture provides a unique assembly strategy with spatiotemporal programmability and opens the door for future cell-cell signaling studies of multiple cell populations or species in synthetic microbiomes. Finally, it is highly desired that the biofabrication of freestanding CM by flows can be scaled up similar to the interfacial electrofabrication of CM using distal electrodes [7]. The capability to fabricate freestanding CM in three-dimensional geometry will increase the surface area of CM for enhanced loading of biomolecules or biological components for more diverse applications [24].

Author Contributions

Khanh L. Ly: Conceptualization, Investigation, Visualization, Writing - Original draft
Piao Hu: Visualization, Writing - Reviewing and Editing
Le Hoang Phu Pham: Validation, Writing - Reviewing and Editing
Xiaolong Luo: Conceptualization, Project administration, Supervision, Writing - Reviewing and Editing

Conflicts of interest

There are no conflicts to declare.

Acknowledgements

This work is supported by the National Science Foundation (CAREER 1553330) and the National Institute of Health (1R15GM129766-01). The authors would like to thank Jabez J. Luo and Josiah J. Luo for proofreading the manuscript.

Notes and References

1. V. Narayanamurthy, Z. E. Jeroish, K. S. Bhuvaneshwari, P. Bayat, R. Premkumar, F. Samsuri and M. M. Yusoff, *RSC Advances*, 2020, **10**, 11652-11680.
2. X. Chen, J. Shen, Z. Hu and X. Huo, *Biomedical microdevices*, 2016, **18**, 104.
3. X. Luo, D. L. Berlin, J. Betz, G. F. Payne, W. E. Bentley and G. W. Rubloff, *Lab on a chip*, 2010, **10**, 59-65.
4. T. Braschler, R. Johann, M. Heule, L. Metref and P. Renaud, *Lab on a chip*, 2005, **5**, 553-559.
5. A. Jafari Sanjari and M. Asghari, *ChemBioEng Reviews*, 2016, **3**, 134-158.
6. X. Chen and J. Shen, *Journal of Chemical Technology and Biotechnology*, 2017, **92**, 271-282.
7. W. Ding, C. Liang, S. Sun, L. He and D. Gao, *Journal of Materials Science & Technology*, 2015, **31**, 1087-1093.
8. J. de Jong, R. G. Lammertink and M. Wessling, *Lab on a chip*, 2006, **6**, 1125-1139.
9. P. J. Kenis, R. F. Ismagilov and G. M. Whitesides, *Science (New York, N.Y.)*, 1999, **285**, 83-85.
10. P. J. A. Kenis, R. F. Ismagilov, S. Takayama, G. M. Whitesides, S. Li and H. S. White, *Accounts of Chemical Research*, 2000, **33**, 841-847.
11. G. M. Whitesides, *Nature*, 2006, **442**, 368-373.
12. Y. Cheng, X. Luo, G. Payne and G. Rubloff, *Journal of Materials Chemistry*, 2012, **22**, 7659-7666.
13. X. Luo, H.-C. Wu, J. Betz, G. W. Rubloff and W. E. Bentley, *Biochemical Engineering Journal*, 2014, **89**, 2-9.
14. D. Kim and D. J. Beebe, *Journal of Applied Polymer Science*, 2008, **110**, 1581-1589.
15. J. Gargiuli, E. Shapiro, H. Gulhane, G. Nair, D. Drikakis and P. Vadgama, *Journal of Membrane Science*, 2006, **282**, 257-265.
16. Y. Uozumi, Y. M. Yamada, T. Beppu, N. Fukuyama, M. Ueno and T. Kitamori, *J Am Chem Soc*, 2006, **128**, 15994-15995.
17. J. B. Orhan, R. Knaack, V. K. Parashar and M. A. M. Gijs, *Microelectronic Engineering*, 2008, **85**, 1083-1085.
18. N. Bhattarai, J. Gunn and M. Zhang, *Advanced drug delivery reviews*, 2010, **62**, 83-99.
19. F. Croisier and C. Jérôme, *European Polymer Journal*, 2013, **49**, 780-792.
20. W. Suginta, P. Khunkaewla and A. Schulte, *Chemical reviews*, 2013, **113**, 5458-5479.
21. T. D. Nguyen, T. T. Nguyen, K. L. Ly, A. H. Tran, T. T. N. Nguyen, M. T. Vo, H. M. Ho, N. T. N. Dang, V. T. Vo, D. H. Nguyen, T. T. H. Nguyen and T. H. Nguyen, *International Journal of Polymer Science*, 2019, **2019**, 7382717.
22. Y. Cheng, X. Luo, J. Betz, S. Buckhout-White, O. Bekdash, G. F. Payne, W. E. Bentley and G. W. Rubloff, *Soft Matter*, 2010, **6**, 3177-3183.
23. Y. Cheng, X. Luo, G. F. Payne and G. W. Rubloff, *Journal of Materials Chemistry*, 2012, **22**, 7659-7666.
24. S. T. Koev, P. H. Dykstra, X. Luo, G. W. Rubloff, W. E. Bentley, G. F. Payne and R. Ghodssi, *Lab on a chip*, 2010, **10**, 3026-3042.
25. D. Xu, S. Hein and K. Wang, *Materials Science and Technology*, 2008, **24**, 1076-1087.
26. E. Salehi, P. Daraei and A. Arabi Shamsabadi, *Carbohydrate Polymers*, 2016, **152**, 419-432.
27. J. Li, S. Wu, E. Kim, K. Yan, H. Liu, C. Liu, H. Dong, X. Qu, X. Shi, J. Shen, W. E. Bentley and G. F. Payne, *Biofabrication*, 2019, **11**, 032002.
28. K. Li, S. O. Correa, P. Pham, C. B. Raub and X. Luo, *Biofabrication*, 2017, **9**, 034101.
29. K. L. Ly, C. B. Raub and X. Luo, *Materials Advances*, 2020, **1**, 34-44.
30. Y.-M. Sun, W. Wang, Y.-Y. Wei, N.-N. Deng, Z. Liu, X.-J. Ju, R. Xie and L.-Y. Chu, *Lab on a chip*, 2014, **14**, 2418-2427.
31. E. Rosella, N. Jia, D. Mantovani and J. Greener, *Journal of Materials Science & Technology*, 2020, DOI: https://doi.org/10.1016/j.jmst.2020.02.059.

32. S. T. Koev, M. A. Powers, H. Yi, L.-Q. Wu, W. E. Bentley, G. W. Rubloff, G. F. Payne and R. Ghodssi, *Lab on a chip*, 2007, **7**, 103-111.
33. D. Du, J. Ding, J. Cai and A. Zhang, *Journal of Electroanalytical Chemistry*, 2007, **605**, 53-60.
34. X. He, R. Yuan, Y. Chai and Y. Shi, *Journal of Biochemical and Biophysical Methods*, 2008, **70**, 823-829.
35. X. Luo, T. Vo, F. Jambi, P. Pham and J. S. Choy, *Lab on a chip*, 2016, **16**, 3815-3823.
36. X. Luo, H. C. Wu, C. Y. Tsao, Y. Cheng, J. Betz, G. F. Payne, G. W. Rubloff and W. E. Bentley, *Biomaterials*, 2012, **33**, 5136-5143.
37. N. Jia, E. Rosella, E. Juère, R. Pouliot, F. Kleitz and J. Greener, *Lab on a chip*, 2020, **20**, 1066-1071.
38. A. Montembault, C. Viton and A. Domard, *Biomacromolecules*, 2005, **6**, 653-662.
39. P. Hu, C. B. Raub, J. S. Choy and X. Luo, *Journal of Materials Chemistry B*, 2020, **8**, 2519-2529.
40. P. L. H. Pham, S. A. Rooholghodos, J. S. Choy and X. Luo, 2018, **2**, 1700180.
41. P. Pham, T. Vo and X. Luo, *Lab on a chip*, 2017, **17**, 248-255.
42. T. Vo, S. B. Shah, J. S. Choy and X. Luo, 2020, **14**, 014108.
43. C. E. Sing and A. Alexander-Katz, *EPL (Europhysics Letters)*, 2011, **95**, 48001.
44. C. Sendner and R. R. Netz, *EPL (Europhysics Letters)*, 2008, **81**, 54006.
45. H. Yang, H. Jussila, A. Autere, H.-P. Komsa, G. Ye, X. Chen, T. Hasan and Z. Sun, *ACS Photonics*, 2017, **4**, 3023-3030.
46. J. Rieppo, J. Hallikainen, J. S. Jurvelin, I. Kiviranta, H. J. Helminen and M. M. Hyttinen, *Microsc. Res. Tech.*, 2008, **71**, 279-287.
47. K. Kocsis, M. Hyttinen, H. J. Helminen, M. B. Aydelotte and L. Módis, 1998, **43**, 511-517.
48. L. H. Phu Pham, L. Bautista, D. C. Vargas and X. Luo, *RSC Advances*, 2018, **8**, 30441-30447.
49. A. Nguyen-My Le, T. T. Nguyen, K. L. Ly, T. D. Luong, M. H. Ho, N. Minh-Phuong Tran, N. Ngoc-Thao Dang, T. Van Vo, Q. N. Tran and T. H. Nguyen, *Polymer Degradation and Stability*, 2020, **180**, 109270.
50. X. Lv, W. Zhang, Y. Liu, Y. Zhao, J. Zhang and M. Hou, *Carbohydr Polym*, 2018, **198**, 86-93.
51. P. Hu, S. A. Rooholghodos, L. H. Pham, K. L. Ly and X. Luo, *Langmuir*, 2020, **36**, 11034-11043.
52. Y. Gu, V. Hegde and K. J. M. Bishop, *Lab on a Chip*, 2018, **18**, 3371-3378.
53. M. P. Tibbe, A. M. Leferink, A. van den Berg, J. C. T. Eijkel and L. I. Segerink, 2018, **3**, 1700200.
54. L.-Y. Chu and W. Wang, 2017, DOI 10.1002/9783527803637.ch12, pp. 253-266.
55. W. Ding, X. Zhu, L. Zou, J. Liu, D. Wang, C. Liang, C. Li and L. He, *International Journal of Heat and Mass Transfer*, 2016, **99**, 822-830.
56. C. S. Thompson and A. R. Abate, *Lab on a chip*, 2013, **13**, 632-635.
57. Y. Zhang, N. E. Benes and R. G. H. Lammertink, *Lab on a chip*, 2015, **15**, 575-580.
58. A. M. Skelley and J. Voldman, *Lab on a chip*, 2008, **8**, 1733-1737.
59. S. He, W. Zhang, D. Li, P. Li, Y. Zhu, M. Ao, J. Li and Y. Cao, *Journal of Materials Chemistry B*, 2013, **1**, 1270-1278.
60. A. Saeed, D. M. R. Georget and A. G. Mayes, *Reactive and Functional Polymers*, 2010, **70**, 230-237.
61. S. Schmidt, M. Zeiser, T. Hellweg, C. Duschl, A. Fery and H. Möhwald, 2010, **20**, 3235-3243.
62. R. Xie, X.-L. Song, F. Luo, Z. Liu, W. Wang, X.-J. Ju and L.-Y. Chu, 2016, **39**, 841-848.
63. L. Liu, X. L. Song, X. J. Ju, R. Xie, Z. Liu and L. Y. Chu, *The journal of physical chemistry. B*, 2012, **116**, 974-979.
64. N. T. Truc, H. H. Minh, L. L. Khanh, V. M. Thuy, V. Van Toi, T. Van Man, H. C. N. Nam, T. N. Quyen and N. T. Hiep, *Surface and Coatings Technology*, 2018, **344**, 664-672.
65. I. Goldberga, R. Li and M. J. Duer, *Accounts of Chemical Research*, 2018, **51**, 1621-1629.
66. M. Mizuno, R. Fujisawa and Y. Kuboki, *J Cell Physiol*, 2000, **184**, 207-213.
67. M. Achilli and D. Mantovani, *Polymers*, 2010, **2**, 664-680.
68. F. Boccafoschi, M. Bosetti, C. Mosca, D. Mantovani and M. Cannas, *Journal of tissue engineering and regenerative medicine*, 2012, **6**, 60-67.
69. R. N. Chen, G. M. Wang, C. H. Chen, H. O. Ho and M. T. Sheu, *Biomacromolecules*, 2006, **7**, 1058-1064.
70. O. C. Santiago, L. Xiaolong and B. R. Christopher, *Journal of Micromechanics and Microengineering*, 2020.
71. R. N. Huynh, M. Yousof, K. L. Ly, F. C. Gombedza, X. Luo, B. C. Bandyopadhyay and C. B. Raub, 2020, **117**, 1826-1838.
72. J. B. Phillips and R. Brown, *Methods in molecular biology (Clifton, N.J.)*, 2011, **695**, 183-196.
73. J. B. Phillips, *Organogenesis*, 2014, **10**, 6-8.
74. X. Luo, C. Y. Tsao, H. C. Wu, D. N. Quan, G. F. Payne, G. W. Rubloff and W. E. Bentley, *Lab on a chip*, 2015, **15**, 1842-1851.
75. W.-L. Hsu, D. W. Inglis, H. Jeong, D. E. Dunstan, M. R. Davidson, E. M. Goldys and D. J. E. Harvie, *Langmuir*, 2014, **30**, 5337-5348.
76. X. Wang, Z. Liu and Y. Pang, *RSC Advances*, 2017, **7**, 29966-29984.
77. C. J. Wolfram, G. W. Rubloff and X. Luo, *Biomicrofluidics*, 2016, **10**, 061301.
78. R. A. Arkowitz, *Cold Spring Harb Perspect Biol*, 2009, **1**, a001958-a001958.
79. X. Wang, J. Atencia and R. M. Ford, *Biotechnology and Bioengineering*, 2015, **112**, 896-904.
80. K. Nagy, O. Sipos, S. Valkai, É. Gombai, O. Hodula, Á. Kerényi, P. Ormos and P. Galajda, 2015, **9**, 044105.
81. J. Diao, L. Young, S. Kim, E. A. Fogarty, S. M. Heilman, P. Zhou, M. L. Shuler, M. Wu and M. P. DeLisa, *Lab on a chip*, 2006, **6**, 381-388.
82. V. V. Abhyankar, M. A. Lokuta, A. Huttenlocher and D. J. Beebe, *Lab on a chip*, 2006, **6**, 389-393.
83. D. J. Webre, P. M. Wolanin and J. B. Stock, *Current Biology*, 2003, **13**, R47-R49.
84. M. M. Salek, F. Carrara, V. Fernandez, J. S. Guasto and R. Stocker, *Nature communications*, 2019, **10**, 1877.
85. T. Ahmed, T. S. Shimizu and R. Stocker, *Nano Letters*, 2010, **10**, 3379-3385.
86. N. Garcia-Seyda, L. Aoun, V. Tishkova, V. Seveau, M. Biarnes-Pelicot, M. Bajénoff, M.-P. Valignat and O. Theodoly, *Lab on a chip*, 2020, **20**, 1639-1647.
87. A. G. G. Toh, Z. P. Wang, C. Yang and N.-T. Nguyen, *Microfluidics and Nanofluidics*, 2014, **16**, 1-18.
88. J. J. VanDersarl, A. M. Xu and N. A. Melosh, *Lab on a chip*, 2011, **11**, 3057-3063.
89. O. C. Amadi, M. L. Steinhauser, Y. Nishi, S. Chung, R. D.

Kamm, A. P. McMahon and R. T. Lee, *Biomedical microdevices*, 2010, **12**, 1027-1041.

90. Y. Liu, W. B. Butler and D. Pappas, *Analytica chimica acta*, 2012, **743**, 125-130.

91. J. Wu, Z. He, Q. Chen and J.-M. Lin, *TrAC Trends in Analytical Chemistry*, 2016, **80**, 213-231.

92. H. J. Kim, H. Li, J. J. Collins and D. E. Ingber, *Proceedings of the National Academy of Sciences of the United States of America*, 2016, **113**, E7-15.

93. J.-M. Prot, A. Bunescu, B. Elena-Herrmann, C. Aninat, L. C. Snouber, L. Griscom, F. Razan, F. Y. Bois, C. Legallais, C. Brochot, A. Corlu, M. E. Dumas and E. Leclerc, *Toxicol Appl Pharmacol*, 2012, **259**, 270-280.

94. D. Huh, D. C. Leslie, B. D. Matthews, J. P. Fraser, S. Jurek, G. A. Hamilton, K. S. Thorneloe, M. A. McAlexander and D. E. Ingber, *Science translational medicine*, 2012, **4**, 159ra147.

95. T. Q. Vu, R. M. de Castro and L. Qin, *Lab on a chip*, 2017, **17**, 1009-1023.

96. L. Keller and M. G. Surette, *Nature reviews. Microbiology*, 2006, **4**, 249-258.

97. H. Somaweera, A. Ibraguimov and D. Pappas, *Analytica chimica acta*, 2016, **907**, 7-17.

98. Z. Wang, I. Lee, T.-J. Jeon and S. M. Kim, *Analytical and Bioanalytical Chemistry*, 2014, **406**, 2679-2686.

99. M.-E. Brett, R. DeFlorio, D. E. Stone and D. T. Eddington, *Lab on a Chip*, 2012, **12**, 3127-3134.

100. T. I. Moore, C.-S. Chou, Q. Nie, N. L. Jeon and T.-M. Yi, *PLOS ONE*, 2008, **3**, e3865.

101. N. Muller, M. Piel, V. Calvez, R. Voituriez, J. Gonçalves-Sá, C.-L. Guo, X. Jiang, A. Murray and N. Meunier, *PLOS Computational Biology*, 2016, **12**, e1004795.

102. C. Y. Tsao, S. Hooshangi, H. C. Wu, J. J. Valdes and W. E. Bentley, *Metabolic engineering*, 2010, **12**, 291-297.

103. J. Li, C. Attila, L. Wang, T. K. Wood, J. J. Valdes and W. E. Bentley, 2007, **189**, 6011-6020.

104. T. Das, S. Sehar, L. Koop, Y. K. Wong, S. Ahmed, K. S. Siddiqui and M. Manefield, *PLOS ONE*, 2014, **9**, e91935.

105. L. F. Cruz, P. A. Cobine and L. De La Fuente, *Appl Environ Microbiol*, 2012, **78**, 1321-1331.

106. M. A. Patrauchan, S. Sarkisova, K. Sauer and M. J. Franklin, *Microbiology (Reading, England)*, 2005, **151**, 2885-2897.

107. S.-H. Yu, F.-L. Mi, Y.-B. Wu, C.-K. Peng, S.-S. Shyu and R.-N. Huang, 2005, **98**, 538-549.

108. L. F. Gómez Chabala, C. E. E. Cuartas and M. E. L. López, *Mar Drugs*, 2017, **15**, 328.

109. L. Loan Khanh, N. Thanh Truc, N. Tan Dat, N. Thi Phuong Nghi, V. van Toi, N. Thi Thu Hoai, T. Ngoc Quyen, T. Thi Thanh Loan and N. Thi Hiep, *Science and Technology of Advanced Materials*, 2019, **20**, 276-290.

110. K. L. Ly, V. Van Toi and T.-H. Nguyen, 7th International Conference on the Development of Biomedical Engineering in Vietnam (BME7), 2020.

111. J. Li and S. Zhuang, *European Polymer Journal*, 2020, **138**, 109984.

112. D. Raafat and H.-G. Sahl, *Microb Biotechnol*, 2009, **2**, 186-201.

113. S. Damiati, U. B. Kompella, S. A. Damiati and R. Kodzius, *Genes (Basel)*, 2018, **9**, 103.

114. P. Cui and S. Wang, *Journal of Pharmaceutical Analysis*, 2019, **9**, 238-247.

115. K. Möller and T. Bein, *Chemistry of Materials*, 2017, **29**, 371-388.

116. J. Florek, R. Caillard and F. Kleitz, *Nanoscale*, 2017, **9**, 15252-15277.

117. Y. Song, Y. Li, Q. Xu and Z. Liu, *Int J Nanomedicine*, 2016, **12**, 87-110.

118. L. Liu, J.-P. Yang, X.-J. Ju, R. Xie, Y.-M. Liu, W. Wang, J.-J. Zhang, C. H. Niu and L.-Y. Chu, *Soft Matter*, 2011, **7**, 4821-4827.

119. W. Wei, L.-Y. Wang, L. Yuan, Q. Wei, X.-D. Yang, Z.-G. Su and G.-H. Ma, *Advanced Functional Materials*, 2007, **17**, 3153-3158.

120. N. Sawtarie, Y. Cai and Y. Lapitsky, *Colloids and Surfaces B: Biointerfaces*, 2017, **157**, 110-117.

121. J. D. Giraldo, V. H. Campos-Requena and B. L. Rivas, *Polymer Bulletin*, 2019, **76**, 3879-3903.

122. K. L. Ly, S. A. Rooholghodos, C. Rahimi, B. Rahimi, D. R. Bienek, G. Kaufman, C. B. Raub and X. Luo, *Biomedical Microdevices*, 2021, **23**, 7.